Marine Geology 430 (2020) 106333

Contents lists available at ScienceDirect

Marine Geology

journal homepage: www.elsevier.com/locate/margo

Invited Research Article

Low-temperature, shallow-water hydrothermal vent mineralization following the recent submarine eruption of Tagoro volcano (El Hierro, Canary Islands)

F.J. González[a,*], B. Rincón-Tomás[b], L. Somoza[a], E. Santofimia[a], T. Medialdea[a], P. Madureira[c], E. López-Pamo[a], J.R. Hein[d], E. Marino[a,e], C. de Ignacio[e], J. Reyes[a], M. Hoppert[b], J. Reitner[f]

[a] Geological Survey of Spain (IGME), Rios Rosas 23, 28003 Madrid, Spain
[b] Georg-August-University Göttingen, Institute of Microbiology and Genetics, Grisebachstraße 8, 37077 Göttingen, Germany
[c] Estrutura de Missão para a Extensão da Plataforma Continental. (EMEPC), Rua Costa Pinto n° 165, 2770-047 Paço de Arcos, Portugal/ Dpt. Geociências e ICT, Univ. Évora, R. Romão Ramalho, 59, Portugal
[d] U. S. Geological Survey (USGS), Pacific Coastal and Marine Science Center, Santa Cruz, CA 95060, USA
[e] Complutense University of Madrid, Faculty of Geosciences, Mineralogy and Petrology Dpt, Jose Antonio 14 Novais 2, 28040 Madrid, Spain
[f] Georg-August-University Göttingen, Geobiology, Göttingen Centre of Geosciences, Goldschmidtstraße 16 3, 37077 Göttingen, Germany

ARTICLE INFO

Keywords:
Tagoro volcano
Low-temperature hydrothermalism
Biomineralization
Ferrihydrite
Submarine eruption
Canary Islands

ABSTRACT

Hydrothermal iron (Fe)-rich sediments were recovered from the Tagoro underwater volcano (Central Atlantic) that formed during the 2011–2012 volcanic event. Cruises in 2012 and 2014 enabled the monitoring and sampling of the early-stage establishment of a hydrothermal system. Degassing vents produced acoustic flares imaged on echo-sounders in June 2012, four months after the eruption. A novel hydrothermal vent system was discovered and sampled in 2014 during a ROV dive. The system is characterized by hornito-like structures and chimneys showing active CO_2 degassing and anomalous temperatures at 120–89 m water depth, and along the SE flank at 215-185 m water depth associated with secondary cones. Iron- and silica-rich gelatinous deposits pooled over and between basanite in the hornitos, brecciated lavas, and lapilli. The low temperature, shallow-water hydrothermal system was discovered by the venting of Fe-rich fluids that produced a seafloor draped by extensive Fe-flocculate deposits precipitated from the neutrally buoyant plumes located along the oxic/photic zone at 50-70 m water depths. The basanite is capped by mm- to cm-thick hydrothermally derived Fe-oxyhydroxide sediment, and contains micro-cracks and degasification vesicles filled by sulfides (mostly pyrite). Mineralogically, the Fe-oxyhydroxide sediment consists of proto-ferrihydrite and ferrihydrite with scarce pyrite at their base. The Fe-rich endmember contains low concentrations of most trace elements in comparison with hydrogenetic ferromanganese deposits, and the sediments show some dilution of the Fe oxyhydroxide by volcanic ash. The Fe-oxyhydroxide phase, with a mean particle size of 3–4 nm, low average La/Fe ratios of the mineralized deposits from the various sampling sites, and the positive Eu anomalies indicate rapid deposition of the Fe oxyhydroxide near the hydrothermal vents. Electron microprobe studies show the presence of various organomineral structures, mainly twisted stalks and sheaths covered by iron-silica deposits within the mineralized samples, reflecting microbial iron-oxidation from the hydrothermal fluids. Sequencing of 16 s rRNA genes also reveals the presence of other microorganisms involved in sulfur and methane cycles. Samples collected from hornito chimneys contain silicified microorganisms coated by Fe-rich precipitates. The rapid silicification may have been indirectly promoted by microorganisms acting as nucleation sites. We suggest that this type of hydrothermal deposit might be more frequent than presently reported to occur in submarine volcanoes. On a geological scale, these volcanic eruptions and low-temperature hydrothermal vents might contribute to increased dissolved metals in seawater, and generate considerable Fe-oxyhydroxide deposits as identified in older hot-spot seamounts.

* Corresponding author.
E-mail address: fj.gonzalez@igme.es (F.J. González).

https://doi.org/10.1016/j.margeo.2020.106333
Received 12 May 2020; Received in revised form 8 July 2020; Accepted 24 August 2020
Available online 29 August 2020

1. Introduction

Hydrothermal activity and mineralization (massive sulfides and Fe-Mn oxyhydroxides) characterize most spreading centers at mid-oceanic ridges and in back-arc basins, usually associated with deep water up to 5000 m water depth (e.g., Rona et al., 1983; Rona, 1986, 2003; Hannington et al., 2005; Pirajno, 2009; Zeng et al., 2012; Cherkashov, 2017); this phenomenon is poorly known in intraplate settings associated with hotspot volcanism. Some examples include Moua-Pihaa volcano and Teahitia volcano in the South Pacific (Stoffers et al., 1993; Hekinian, 2014) and Loihi Seamount in Hawaii (Karl et al., 1988; Edwards et al., 2011). Low-temperature hydrothermal Fe-oxyhydroxide deposits have been reported to occur at intraplate islands and seamounts in eastern Papua New Guinea shallow waters (near-shore environments) (e.g., Pichler et al., 1999), eastern (Alt, 1988) and western (Hein et al., 1994) Pacific seamounts, and the southern California continental margin (Hein et al., 2005). Low-temperature hydrothermal iron laminated mounds and chimneys have been reported at the Jan Mayen Vent Fields on the Arctic Mid-Ocean Ridge (Moeller et al., 2014; Johannessen et al., 2017). Hydroxides precipitate directly on the seafloor from diffuse low-temperature (from 10 to 100 °C) hydrothermal fluid emissions around vents by mixing with cold seawater, and commonly reveal structures indicative of a biogenic origin (Juniper and Tebo, 1995; Emerson and Moyer, 2002; Emerson et al., 2010). In fact, microaerophilic iron-oxidizing bacteria (FeOB) are well known to precipitate iron in these environments, producing stalks and sheaths rich in Fe oxyhydroxides commonly found as iron-rich mats (Alt, 1988; Jannasch, 1995; Van Dover, 2000; Halbach et al., 2001; Hanert, 2002; Canet et al., 2005; Emerson et al., 2007, 2010; Hein et al., 1999, 2008a). Bacteria and archaea involved in other cycles, e.g. in methane and sulfur cycles, are also commonly found associated with these iron-oxide mats produced from low-temperature hydrothermal vents. The presence of microorganisms favors the precipitation of iron hydroxides, but also opal-A and other minerals (e.g. pyrite) (Fortin et al., 1997; Boyd and Scott, 2001; Kelley et al., 2002; Edwards et al., 2011).

The rapid diminution of quality and quantity of land-based world resources has put a major thrust on the exploration and exploitation of minerals in the deep-ocean settings. Security of mineral supply has been identified by governments and industry as a priority challenge facing the raw materials sector, reflecting societies growing demand for an ever-increasing number and quantity of elements and minerals that supply the green energy and technology markets (European Commission, 2017; Sovacool et al., 2020). Recent investigations addressed the connections between microbial action and their role in the accumulation of these critical metals in fossil hydrothermal mineralized deposits (e.g., Tornos et al., 2015, 2018; Movahednia et al., 2020). This knowledge addresses the need to have a better understanding of submarine minerals, their ecological and environmental settings, metallogenic potential, and exploration technologies to accurately determine the geographical distribution and element concentrations of varied marine deposits.

Fe oxyhydroxides are particularly important constituents of marine sediments in volcanically active coastal areas (Hanert, 2002), such as those formed at the Tagoro eruptive event in 2011–2012 (González et al., 2014; Somoza et al., 2017). During the volcanic episode, fluid emissions enriched in CO_2, CH_4, H_2S, Si, Fe^{2+} and other elements, affected the pH, temperature and composition of local seawater and therefore marine life (Fraile-Nuez et al., 2012; Santana-Casiano et al., 2013). The biologically mediated transformation of aqueous ions into amorphous and crystalline materials gave rise to biominerals around the vent sites that formed these hydrothermal deposits (González et al., 2014, 2017). The low-crystalline nature of Fe-oxyhydroxide minerals makes them good scavengers for metals and, therefore, the Fe mineralization is an important removal mechanism from seawater for many trace elements (Hein et al., 1997, 2000).

This work is based on a study of unique samples of Fe-oxyhydroxide mineralization retrieved from lava ponds found at secondary cones on the flank, and hornito-like structures at the summit of Tagoro volcano (El Hierro Island) (Fig. 1). Physico-chemical and acoustic properties of fluids expelled during the hydrothermal and degassing processes have been studied. At the same time, ROV underwater videos were analyzed and interpreted. The characterization of the mineralization process discussed here is based on morphology, structure, micro-texture, mineralogy, and chemistry of the samples. Illumina next generation amplicon sequencing of 16S rRNA genes of prokaryotes was used to support the characterization and identification of microbial biomineralization. This novel low-temperature and shallow-water hydrothermal system represents a natural laboratory to study the temporal and spatial evolution of hydrothermal mineralization and their related microbial community (microbiota). The results of this study open new possibilities for recognizing analogs of ancient Fe-oxyhydroxide biomineralization that occurred in similar environments of intraplate volcanic islands or seamounts, which may be preserved in the geological record on Pacific or Atlantic seamounts (Hein et al., 1994; Marino et al., 2019) and in terrestrial deposits such as the Troodos

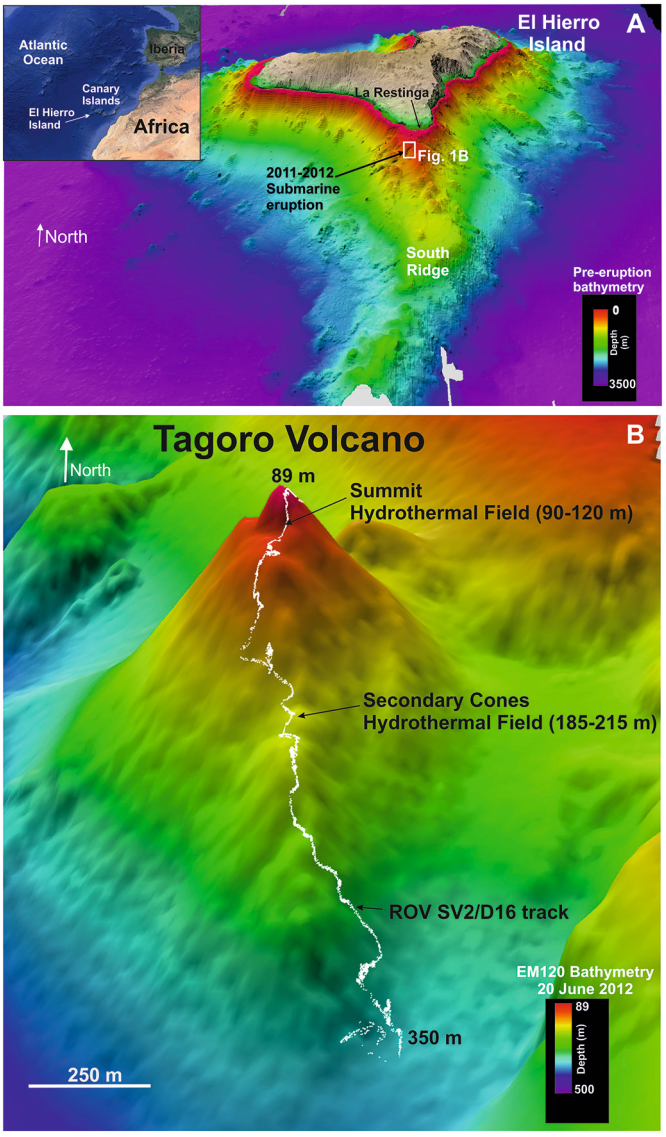

Fig. 1. A) Location of the Canary Islands and 3-D digital terrain model of the El Hierro Island before the 2011-2012 eruption event. B) Three-dimensional multibeam bathymetric image (Simrad EM12-120S) of Tagoro volcano on 20 June 2012. Fledermaus visualization of the volcano morphology with location of ROV track and hydrothermal vent fields. Viewing direction is from the South.

Ophiolite (Robertson, 1975). In addition, these Fe oxyhydroxides could be key for mineral prospecting, as a geochemical pathfinder to economic hydrothermal deposits.

2. Regional setting and study area

The Canary Archipelago (NE Central Atlantic, Fig. 1) comprises the Canary Volcanic Province (CVP) that is made up of seven major islands and numerous volcanic edifices and seamounts. The CVP is characterized by significant and long-lasting (since Early Cretaceous) intraplate volcanism that roughly progressed from east to west from about 23 to 15 million years (Ma) ago for the eastern islands of Lanzarote and Fuerteventura to 1.1 Ma for the westernmost islands of La Palma and El Hierro (Staudigel et al., 1986; Guillou et al., 1996; Carracedo et al., 2002; Ancochea, 2004; Van den Bogaard, 2013). It is widely accepted that the origin of the volcanism can be attributed to a thermal anomaly in the mantle or hot spot (Schmincke, 1982; Hoernle et al., 1991; Hoernle and Schmincke, 1993; Carracedo et al., 1998; Carracedo, 1999; Geldmacher et al., 2001, 2005; Longpré et al., 2009; Deegan et al., 2012), with the predominance of alkaline sodic oceanic island basalts (OIB).

El Hierro Island is the westernmost and youngest island of the Canary Archipelago (Fig. 1A) (Guillou et al., 1996). This island is presently in an early phase of shield-building, with scant Holocene subaerial eruptive activity, when compared with neighboring islands (Carracedo et al., 2015). The shape and architecture of El Hierro is controlled by a three-arm rift system and by the scars of several massive gravitational landslides that give rise to vast embayments with almost vertical escarpments (León et al., 2017, 2019). The volcanic rifts continue offshore. The southern ridge, about 40 km long, hosts volcanic rocks dated as Cretaceous, which probably belong to an older seamount (Van den Bogaard, 2013).

In July–October 2011, more than 12,500 small earthquakes were detected in El Hierro Island with minor surface deformation and gas emissions (López et al., 2012). On October 10, very shallow earthquakes, continuous harmonic tremor, dead fish, and patches of pale-colored water indicated the onset of a submarine eruption at about 300 m water depth, about 5 km distance from the town of La Restinga (Carracedo et al., 2012). It was the first time a submarine eruption was observed and monitored in the Canary Islands (Fig. 1S). The El Hierro eruption formed a new submarine cone by the end of October 2011, named Tagoro volcano (Fig. 1B). The submarine volcano edifice rises on the southern rift of El Hierro from 350 m depth up to 89 m below sea level. The erupted material consists of basanite lava balloons and rock fragments that correspond to pale-colored, highly vesicular, glassy material, surrounded by dark basanite. The eruption continued, as monitored by seismic tremors, throughout late February when seismicity was drastically reduced and until 6 March 2012, when the red alert originally issued by National Geographic Institute of Spain (IGN) was removed. After this eruption, the system produced hydrothermal vents.

Several relatively ancient and modern hydrothermal systems have been discovered and studied onshore and offshore in the CVP revealing a great diversity of hydrothermal activity. Evidence of hydrothermal activity onshore are not abundant, but several hydrothermal systems have been studied in Tenerife, Gran Canaria, and Lanzarote islands. In Lanzarote Island, the presence of hydrothermal alteration within the lavas of the Timanfaya eruption (1736–1730), characterized by high proportions of quartz and opal, suggests the effective circulation of hot fluids. The source of these fluids would be located deeper in the island, where silica was dissolved from sandstones and radiolarites, moving towards the surface as $Si(OH)_4$ colloids (Carmona et al., 2009). In Gran Canaria Island, low-temperature steam fumaroles produced epithermal alteration during the Miocene, with clay minerals, zeolites, and adularia mineralization in intracaldera tuffs of Tejeda caldera (Donoghue et al., 2008). Hydrothermal mineralization has also been found in the NW of the Anaga Massif (Tenerife Island) hosted in mid-upper Miocene ankaramite basalts (Rodríguez-Losada et al., 2000). The mineralization consists of major jasper (quartz and opal) and celadonite, in association with minor hematite, magnetite, Fe ± Ca, Mg carbonates, kaersutite, calcite, and traces of ilmenite, always associated with magnetite. Considering the occurrence of celadonite, it was proposed that heated seawater was the main mechanism of alteration, probably mixed with mineralizing fluids (Rodríguez-Losada et al., 2000). This mineralization is similar to that found in other Canary Islands, e.g. Fuerteventura (Mangas et al., 1994) and La Palma (Schiffman and Staudigel, 1994).

Offshore hydrothermal systems have been discovered recently at both shallow- and deep-water locations. Exploration in the Canary Basin revealed and documented the occurrence of hydrothermal vent complexes and volcanic cones at 5200–4800 m water depth related to recent volcanic and intrusive activity 500 km west of the Canary Islands (Medialdea et al., 2017). These volcanoes, which must be among the deepest in the world, consist of ocean island basalts-type (OIB) basanites with an outer ring of blue-green hydrothermal Al-rich smectite muds (Fe-beidellite-montmorillonite). The Subvent hydrothermal-volcanic complex constitutes the first modern system reported in deep-water oceanic basins related to intraplate hotspot activity. The magmatic events that occurred between 1.6 Ma and 25 ka, and the OIB nature of the lava and tephra sampled in the deep-water volcanoes, suggest the presence of a mantle anomaly in the area during the Quaternary (Medialdea et al., 2017). Other evidence of recent or fossil hydrothermal vents have been reported in the Canary Island Seamount Province (EMODnet-Geology, 2020; MINDeSEA, 2020). Holocene massive, veinlets, and disseminated barite deposits and associated fauna (genus *Abyssogena*) were recovered at 3100 m water depth in Henry Seamount (South El Hierro Island) (Klügel et al., 2011). Pyrite and Fe-oxyhydroxide mineralized deposits related to volcanic-associated hydrothermal events were found on Tropic and Drago seamounts located at the SW edge of the CVP (IGME, 2014; Marino et al., 2019).

Shallow-water hydrothermal fields were discovered in 2014 on Tagoro volcano during the SUBVENT-2 expedition, and mapped over two areas at the mid flank (215–185 m water depth) and summit of the volcano (120–90 m water depth) (Somoza et al., 2014). The underwater volcano has been cooling and degassing since March 2012, supporting fluid exchange between the volcanic edifice and the ocean. Hydrothermal vents have been acting as discharge sites for warm-spring fluids and potential recharge sites for seawater. As a consequence, Fe-oxyhydroxide sediments have accumulated in the vicinity of the warm vent sites and specific vent fauna communities have developed (González et al., 2014, 2017; Somoza et al., 2017; Danovaro et al., 2017). The emissions of CO_2 gas to the water column and carbonate alkalinity from El Hierro accounted for 60% and 40%, respectively, of the pH change in local seawater around the main cone of the volcano (Santana-Casiano et al., 2016).

3. Methodology

3.1. Cruises and sampling

Detailed information about the geophysical and sampling techniques can be found in Table 1 and the supporting information (Table 1S). Sample recovery and geophysical surveying were conducted on a cruise with the Spanish R/V *Sarmiento de Gamboa* on 4 April 2014 (SUBVENT-2), and the remotely operated vehicle (ROV 6000) *Luso* (EMEPC, Portugal), after the eruption and during the hydrothermal-degasification stage. Two geophysical surveys used the Spanish R/V *Sarmiento de Gamboa* (GAIRE 2011) in November–December 2011 during the eruptive event, and the Spanish R/V *Hespérides* in 2012 (AMULEY-ZEE 2012) at the end of the eruptive event and onset of hydrothermalism. In addition, non-mineralized core sediment samples were collected by gravity coring with a 5 m long barrel west of El Hierro Island at 4845 m water depth aboard the R/V *Hespérides* in 2013 (MAEC-SUBVENT-1 2013). Non-mineralized sediments are used as regional background

Table 1
Data set of location and the most relevant characteristics of the ROV stations and the gravity core selected for this study.

Sample ID	Water depth (m)	Latitude (N)	Longitude (W)	Description
SV2/D16-R1	346	27.6162	-17.9900	Non-mineralized basanite lava, 2011-2012 eruptive event
SV2/D16-R5ox (Fe-ox)	213	27.6175	-17.992	Hydrothermal mineralization, Fe oxyhydroxides and silicates patina
SV2/D16-R5 (bedrock)				Basanite, scoriaceous lava fragment
SV2/D16-C6ox (Fe-ox)	205	27.6178	-17.9923	Hydrothermal mineralization, Fe oxyhydroxides patina
SV2/D16-C6 (bedrock)				Basanite, scoria fragments
SV2/D16-R9ox (Fe-ox)	118	27.6144	-17.9934	Hydrothermal mineralization, hornito top flocculent gelatinous Fe oxyhydroxides
SV2/D16-R9 (bedrock)				Basanite mafic lava spatter from the top of a hornito-like chimney
SV2/D16-N10	118	27.6194	-17.9932	Seawater collected at the base of the hornito
SV2/D16-R11ox (Fe-ox)	115	27.6195	-17.9933	Hydrothermal mineralization, hornito base flocculent gelatinous Fe oxyhydroxides
SV2/D16-R12ox (Fe-ox)				
SV2/D16-R11 (bedrock)				Basanite mafic lava spatter from the base of a hornito-like chimney
SV2/D16-R12 (bedrock)				
SV2/D16-N14	97	27.6201	-17.9934	Seawater collected at Tagoro summit
SV2/D16-R15ox (Fe-ox)	90	27.6203	-17.9937	Hydrothermal mineralization, fissure with CO_2 anomaly and thin cover of hydrothermal Fe oxyhydroxides
SV2/D16-R15 (bedrock)				Basanite lava from a fissure zone with CO_2 anomaly and thin cover of hydrothermal Fe-Mn oxyhydroxides
SV2/D16-N16	90	27.6203	-17.9937	Seawater collected in a fissure zone
SV1/TG16 (0-5 cm)	4845	27.3088	-22.7128	Non-mineralized carbonate core sediment, west of El Hierro Island
SV1/TG16 (248-255 cm)				Non-mineralized siliceous core sediment, west of El Hierro Island

samples.

The Tagoro volcano was acoustically surveyed using the Konsberg EK60 split-beam scientific echo-sounder during the Amuley cruise on 19–20 June 2012, aboard the R/V *Hésperides*, almost five months after the eruption ceased. This echosounder was operated at 38 kHz and 120 kHz with amplification gains ranging between 25–27 dB to identify the acoustic plumes. Digital files were imported by means of the Echoviewer software. The backscatter scale of the echograms ranged from −80 dB to 5 dB (blue colors are minimum whereas red are maximum backscatter values). On 19 June 2012, a survey along the SW side of the volcano (Fig. 2A) and on 20 June 2012 a sequence of tracks crossing the Tagoro volcano in an E–W direction were performed, at a ship speed of 5 knots (Fig. 2B). Below, we refer to the hydro-acoustic plumes as *flares* due to their shape on echograms (Fig. 2) to clearly distinguish them from geochemical/turbidity anomalies in the water column related to hydrothermal vents (Greinert et al., 2006). The Konsberg EK60 echo-sounder data were processed using Echoview software in order to transform data from time to real position. The PHF mode data of the parametric echosounder was transformed using Kingdom Suite software.

Submersible observations and sampling of hydrothermal vent sites, seawater, and microbial mineralized sediments and rocks were carried out using the ROV *Luso* (Fig. 3). The *Luso* is equipped with (i) a high definition camera (1024x1024 pixel digital still camera); (ii) two robotic manipulators for biological/geological samples; (iii) a CTD which measures electric conductivity (mS/cm), temperature (°C), depth (m), fluorescence (μg/L) and turbidity (FTU); (iv) CO_2 (μatm) and O_2 (mg/L and % sat.) sensors; and (v) four Niskin bottles for water samples of 2.2 L each. The track of the ROV was planned using previous multibeam mapping in order to cross the former 2011–2012 eruptive centers from ca. 380 m water depth to their summit located at ca. 89 m water depth (Figs. 1B and 3). Observations were made by TV camera from an altitude of 0.5–5 m above the seabed moving at the speed of approximately 1 kt (0.5 m/s) or slower. Microbial mat, rock, and seawater sampling was accomplished using the ROV mechanical arm selecting the sampling sites from the underwater images (Fig. 3 and Table 1). All samples were immediately stored at room temperature (petrographic, mineralogical, geochemical analysis), 4 °C (water, sediments), and − 80 °C (environmental DNA analysis). Subsequently, we conducted detailed analyses of selected sample materials from ROV sampling stations, characterized by different types of venting activity that were identified during the dive (Fig. 3).

3.2. Laboratory analysis

Samples used for further laboratory analysis were recovered from the summit hydrothermal field (SV2/D16-R9, SV2/D16-N10, SV2/D16-R11, SV2/D16-R12, SV2/D16N14, SV2/D16-R15, SV2/D16-N16), secondary-cones hydrothermal field (SV2/D16-R5, SV2/D16-C6), and the base of the volcano (SV2/D16-R1) (Fig. 3). Selected samples of soft and friable mineralized deposits, mineralized microbial mats, bedrock, and nonmineralized sediments were studied in the General Laboratories of the Geological Survey of Spain (IGME), the Spanish National Centre for Electron Microscopy (ICTS) of the Complutense University of Madrid (UCM), the Geoscience Centre of the GeorgAugust-University Göttingen, and the Pacific Coastal and Marine Science Center of the United States Geological Survey (USGS).

3.2.1. Mineralogy and Geochemistry

Small fractured pieces broken from vent site samples SV2/D16-R5, SV2/D16-C6, SV2/D16-R9, SV2/D16-R11, SV2/D16-R12, and SV2/D16-R15 (Table 1) were mounted on stubs and sputter-coated with gold before being examined on a JEOL JSM 6400 (JEOL, Tokyo, Japan) scanning electron microscope (SEM). This study produced 116 SEM photomicrographs and 198 microanalyses that were taken from these samples. Mineral identification relied on the morphology of the precipitates and element analyses as determined from energy dispersive X-ray (EDX) analysis on the SEM; analyses were conducted with an accelerating voltage of 20 kV and at working distance of 10 mm to ensure optimum imaging and minimize charging and sample damage.

Electron probe micro analysis (EPMA) and petrographic studies were carried out on 100 μm-thick polished sections. The samples were first thoroughly examined by transmitted and reflected light microscopy, and the internal structure was described, outlined and photographed. Multi-elemental spot analyses and mapping of mineral phases and textural features were carried out using electron probe micro analysis (EPMA) with a JEOL JXA-8900 M Superprobe (JEOL, Tokyo, Japan) operating at 15 to 20 kV and 50 mA and fitted with wavelength dispersive spectrometers (WDS). Back-scattered electron images were also obtained at this facility. Standards included pure metals and synthetic and natural minerals from international suppliers.

Bulk mineralogical X-Ray Diffraction (XRD) diffractograms from 2θ = 2–60° in 0.005 steps were obtained for the biomineralized samples and the volcanic bedrocks using X'PERT PRO of PANalytical (Philips Analytical, Almelo, The Netherlands), Cu-Kα radiation (40 kV and 40 mA) with graphite monochromator, software High Score version

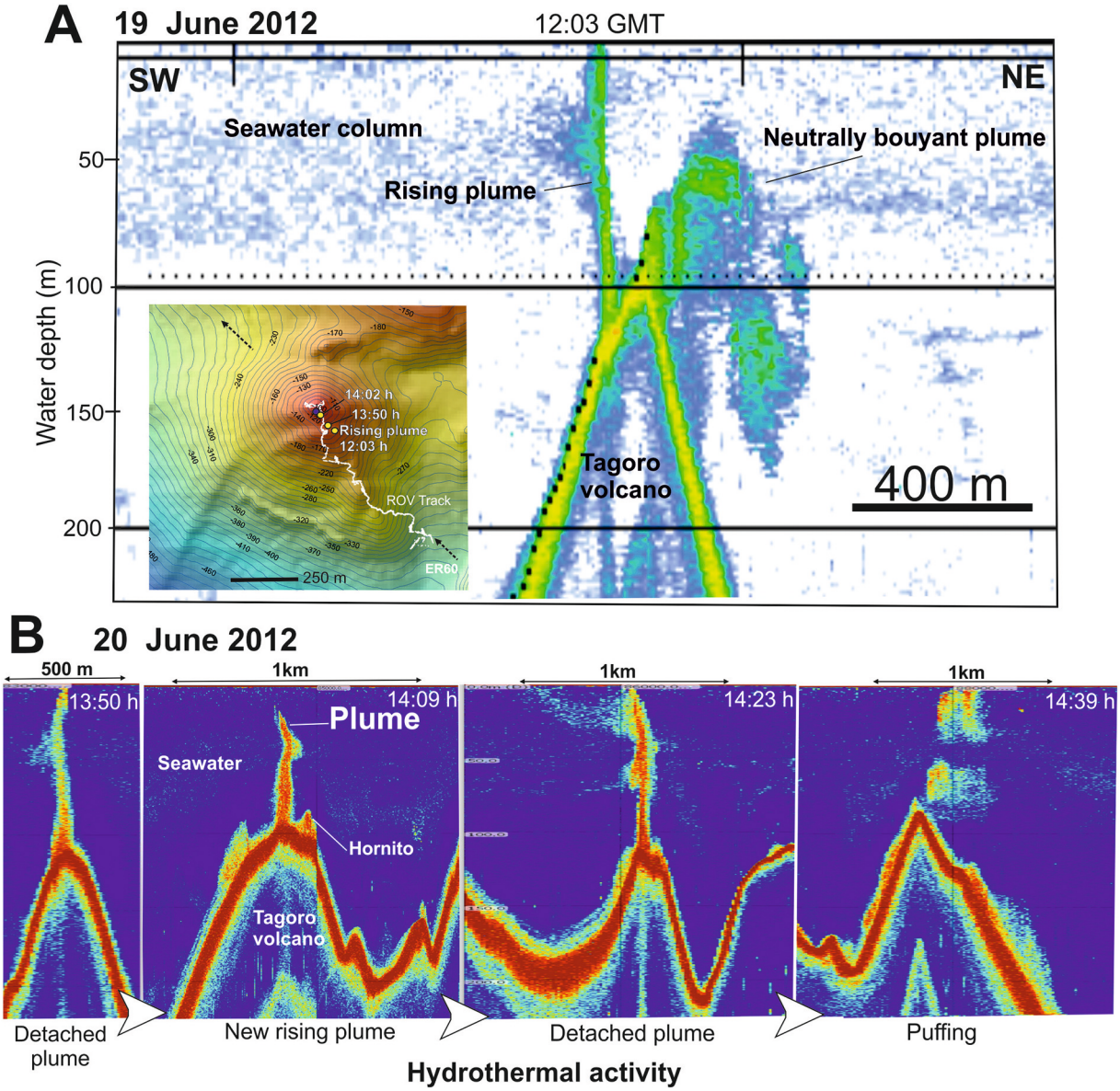

Fig. 2. A) Echogram from Konsberg EA60 (green is high backscatter and blue low backscatter) taken 19 June 2012 after the eruption ceased showing two high-acoustic backscatter flares rising from the summit (see text for further discussion). B) Sequence of flares identified the 20 June 2012 almost five months after ceased the eruption on the summit of the volcano. Images were recorded every 15 min and taken at ship speed of five knots. See text for further explanation. Note that no bent flares were detected this day. (For interpretation of the references to colour in this figure legend, the reader is referred to the web version of this article.)

3.0.4 and ICDD and COD data bases.

The biomineralized samples, volcanic bedrock, and core sediments were prepared and analyzed separately in order to define their bulk chemical composition for major, minor and trace elements by a combination of different technics (Table 3). X-Ray Fluorescence (XRF) using a MagiX of PANalytical instrument (XRF, Philips Analytical, Almelo, The Netherlands) with Rh x-ray tube and Major software (PTE-RX-001 Ed. 3). Si, Al, Fe, Ca, Ti, Mn, K, Mg, and P were determined from borate fused beads. Minor and trace elements in bedrock samples and non-mineralized sediments were determined by XRF analyses on pressed powder pellets made from 8 g of sample, using Pro-Trace software. After digestion of mineralized samples with HF, $HClO_4$, and HNO_3, samples were dried and dissolution of the residue with completed using 7% HNO_3. Ag, As, Ba, Be, Cd, Co, Cr, Cu, Mo, Ni, Pb, Sb, Se, Th, Tl, U, V and Zn were determined with Inductively Coupled PlasmaMass Spectrometry (ICP-MS) in an AGILENT 7500ce instrument (Agilent Technologies, Santa Clara, CA, USA). Li, Nb, Rb, Sc, Sr and W were determined by Inductively Coupled Plasma-Atomic Emission Spectroscopy (ICP-AES) in a VARIAN VISTA-MPX (Varian Analytical Instruments, Mulgrave, Australia). Sodium was measured using Atomic Absorption Spectrophotometry (AAS; mode emission) with a VARIAN-220 FS (Varian Analytical Instruments, Mulgrave, Australia). Mercury was determined by atomic absorption AAS (cold vapor; VARIAN 220 FS) according the method EPA 7471 "Mercury in solid or semisolid waste". The bulk REY (rare earth elements plus yttrium) concentrations of samples were determined by ICP-MS, in an AGILENT 7500ce instrument. Loss on ignition (LOI) was determined by calcination at 950 °C and S was measured in ELTRA CS-800 equipment. (Haan, Germany). Total Organic Carbon (TOC) was calculated by subtracting the TIC obtained by calcination at 550 °C from the Total TC values measured in ELTRA CS-800 equipment. The standard reference materials SO-1 (CCMET), GSP-1 (USGS) and BCR-1 (USGS) and the participation in the GeoPT programme of the International Association of Geoanalysts (a proficiency test for laboratories engaged in the analysis of geological materials) were used to test the analytical procedure for element determinations. Reproducibility based on duplicate samples

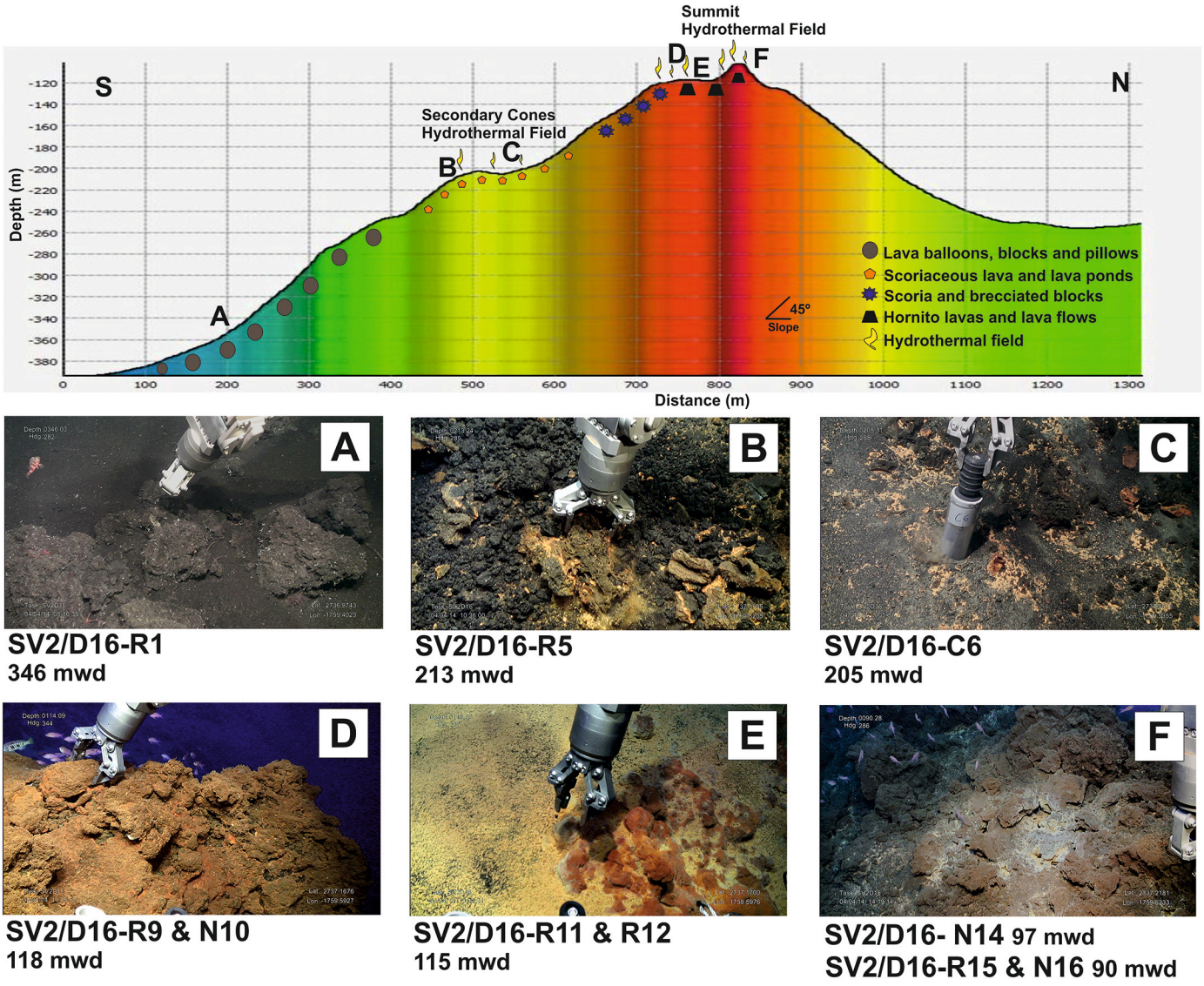

Fig. 3. South-North profile of Tagoro volcano showing distribution of volcanic hydrothermal products and the location and ROV views of sampling stations for basanite lavas at the base of volcano (A), hydrothermal mineralization and seawater in the secondary cones hydrothermal field (B and C) at 230-185 m water depth (mwd), and the summit hydrothermal field (D, E and F) at 120-89 mwd.

was better than 10% for all REY and better than ± 5% for major and trace elements. The Ce anomaly (Ce*) was calculated as Ce* = Log (Ce/(2/3La + 1/3Nd)), all values normalized to Post-Archean Australian Shale (PAAS, Taylor and McLennan, 1985) and Chondrite (Palme et al., 1981). Eu anomalies were calculated from PAAS-normalized data using the equation 2Eu/(Sm + Gd).

Oxidation-reduction potential (ORP) and pH values of seawater from the Niskin bottles were measured on-site with Hanna portable instruments (HI 9025). Seawater was filtered with syringe filters of cellulose acetate (0.45 µm pore), acidified with distilled nitric acid (HNO_3), and stored at 4 °C before further analysis. Dissolved metals in seawater such as Fe and Mn were analyzed using ICP-MS (ICP-MS, Agilent 7500ce equipment), based on the EPA 200.8 method. Method accuracy and precision was checked by external standards (MIV, EPA, NASC, CASS). The precision was better than 5% RSD (Relative Standard Deviation) and the accuracy better than 4%.

3.2.2. Iron stable isotopes

Fe-oxyhydroxide samples were digested in HNO_3, HF, and H_2O_2 (3:2:1) for at least 24 h on a hot plate at 120 °C and the obtained solution was evaporated until dryness at 70 °C. The dried residues were digested using a mixture of concentrated HNO_3 and H_2O_2 (ratio 1:1) at 120 °C for at least 3–4 h and evaporated to dryness and was subsequently re-fluxed in HCl and HNO_3 (3:1) for at least 3 h at 120 °C and finally dissolved in 7 mol L^1 HCl + 0.001% H_2O_2 for ion exchange separation. The acids (HNO_3 and HCl) used in this study were purified by sub-boiling distillation in quartz stills or were purchased in suprapur quality. Other reagents were of suprapur quality. All solutions and dilute acids were prepared using 18 MΩ grade water (EMD Millipore, MA, USA). Iron isotope measurements were performed on a Thermo-Scientific Neptune Plus MC-ICP-MS at the Leibniz University Hannover, Germany. The Fe isotopic compositions were analyzed in the high mass resolution mode to resolve isobaric interferences of $^{40}Ar^{14}N^+$, $^{40}Ar^{16}O^+$, and $^{40}Ar^{16}OH^+$ on ^{54}Fe, ^{56}Fe, and ^{57}Fe (Weyer and Schwieters, 2003) and the standard-sample bracketing method was applied in combination with external element doping for mass bias correction. For the latter, the 5 mg L^{-1} Ni standard NIST 986 (National Institute of Standards and Technology, Gaithersburg, MA, USA) was doped to Fe isotope standard IRMM-014 (Institute for Reference Materials and Measurements, Geel, Belgium) for mass-bias correction (Oeser et al., 2014). The Fe isotope standard and the samples were diluted with 2% HNO_3 to yield a concentration of 7 mg/L Fe. The

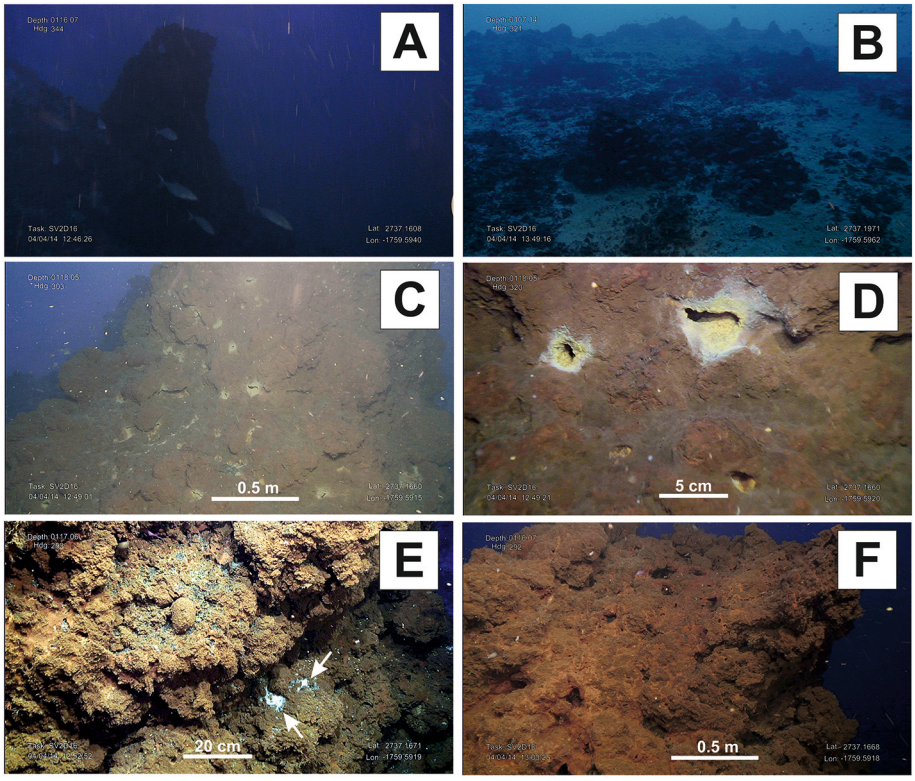

Fig. 4. ROV images of the hornitos-like structures at the summit hydrothermal field of Tagoro volcano. A) Deepest hornito formed by 5 m tall conical-like mafic lava spatter composed of lava blocks covered with orange-yellow hydrothermal deposits (118 m water depth). B) View of different hornitos at the summit and flocculent hydrothermal sediments covering the seafloor. C and D) Details of whitish-yellow patches of oxides around active vent conduits at the base of the deepest hornito. E) Whitish patches with flocculent-filamentous texture (arrows) on the surface of the hornito probably formed by sulfur-oxidizing bacteria colonies. F) Patches of rust-colored Fe oxyhydroxides covering the surface of the black volcanic rocks on top of deepest hornito. (For interpretation of the references to colour in this figure legend, the reader is referred to the web version of this article.)

sample was analyzed at least three times and the mean δ^{56} and δ^{57} Fe values reported relative to IRMM-014.

The uncertainty is represented by 2SD based on three different analysis.

3.2.3. DNA extraction and Illumina MiSeq 16s rDNA gene sequencing

An orange layer covering sample SV2/D16-R12 was carefully removed. Total DNA was isolated with a Power Soil DNA Extraction Kit (MO BIO Laboratories, Carlsbad, CA). All steps were performed according to the manufacturer's instructions. Bacterial and archaeal amplicons of the V3–V4 region were generated with the primer sets S-D-Bact0341-b-S-17/S-D-Bact-0785-a-A-21, and Arch514Fa/archaeal reverse primer, respectively (Klindworth et al., 2013; Wemheuer et al., 2019). The polymerase chain reaction (PCR) mixture for bacterial DNA amplification contained 1 U Phusion highfidelity DNA polymerase (Biozym Scientific, Oldendorf, Germany), 5% dimethyl sulfoxide (DMSO), 0.2 mM of each primer, 200 µM deoxynucleotides (dNTPs) solution mix, 0.15 µL of 25 mM $MgCl_2$ and 25 ng of isolated DNA. The PCR protocol for bacterial DNA amplification included (i) initial denaturing for 1 min at 98 °C; (ii) 25 cycles of 45 s at 98 °C, 45 s at 60 °C, and 30 s at 72 °C; and (iii) a final extension at 72 °C for 5 min. The PCR reaction mixture for archaeal DNA amplification was similarly prepared but contained instead 1 µL of 25 mM $MgCl_2$ and 50 ng of isolated DNA. The PCR protocol for archaeal DNA amplification included (i) initial denaturing for 1 min at 98 °C; (ii) 10 cycles of 45 s at 98 °C, 45 s at 63 °C, and 30 s at 72 °C; (iii) 15 cycles of 45 s at 98 °C, 45 s at 53 °C, and 30 s at 72 °C; and (iv) a final extension at 72 °C for 5 min.

PCR products (ca. 500 bp) were purified using the GeneRead Size Selection Kit (QIAGEN GmbH, Hilden, Germany). Further Illumina PE sequencing and following processing of the sequence data were performed in the in the Göttingen Genomics Laboratory (Göttingen, Germany) as described by Rincón-Tomás et al. (2019), but in this case sequences were clustered at 97% sequence identity to operational taxonomic units (OTUs).

4. Results

4.1. Sampling sites and sample suite

Multibeam bathymetry taken after the eruption ceased shows a volcano formed with a principal cone with a summit at ca. 89 m water depth and flanks with slopes ranging between 25 and 35°, and secondary cones following a NW–SE trend along the southeastern flank (Somoza et al., 2017). Two areas of hydrothermal activity were identified during the dive operations: One at the summit (120–89 m water depth) and the other area at the mid-southeast flank (215–185 m water depth) of Tagoro volcano (Fig. 1B).

4.1.1. Summit hydrothermal field

The echogram taken on 19 June 2012, almost five months after the cessation of the volcanic eruption, shows several hydro-acoustic flares rising from the summit of the Tagoro volcano as evidence for hydrothermal plumes (Fig. 2A). The echogram taken in a SE–NW direction showed two main flares: 1) a vertical 110 m high flare rising from SW of the summit reaching the sea surface, and 2) a flare rising from the NW side of the summit but bending at about 40 m below the sea surface, forming a lobe of high-backscatter (5 dB) pointing to the seafloor (Fig. 2A). The two flares were detached at different water depths, forming horizontal plumes characterized by medium backscatter values (−40 dB) slightly higher than seawater (−80 dB) (Fig. 2A). Short-term variations of the activity of the plumes were observed during the expedition. On 20 June 2012, a sequence of echograms was taken every 15 min in order to identify the behavior the hydrothermal plume (Fig. 2B). The first image (13:50 h) showed a flare rising from the seafloor at the summit to the sea surface. The flare was slightly detached at its upper part. The second image (14:09 h) taken only 19 min later showed a new flare released from the seafloor but without reaching the sea surface. The third image (14:23 h) showed that the new flare had reached the sea surface, and again began to be detached at different points. The last image taken 30 min after the new flare was released shows that the flare became dispersed (14:39 h).

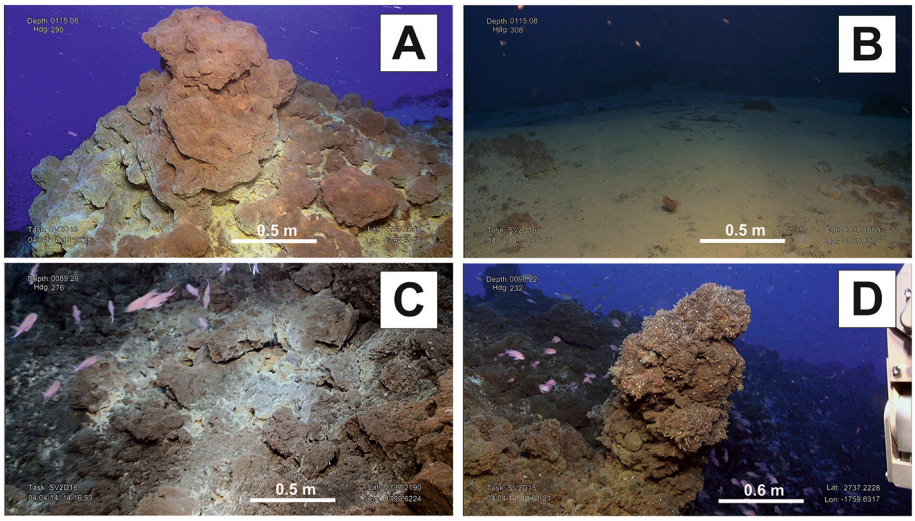

Fig. 5. ROV images of the shallowest hornitos and hydrothermal mineralization at the summit of the Tagoro volcano. A) Shallow hornito (115 mwd) formed by 2 m tall pyramid-like mafic lava spatter composed of lava blocks covered by orange-yellow oxyhydroxide sediment and active emission of CO_2 during the survey. B) Extensive Fe-oxyhydroxide loosely packed deposit on summit of Tagoro volcano. C) Fissure on top of volcano (89 mwd) with emissions of CO_2 and surrounded by Fe-(Mn) oxyhydroxides and opal-A mineralization. D) A columnar mafic lava spatter chimney (98 mwd) composed of lava blocks covered by Fe oxyhydroxides. (For interpretation of the references to colour in this figure legend, the reader is referred to the web version of this article.)

ROV dive SV2/D16 at the summit of the underwater Tagoro volcano revealed extensive Fe-mat deposits overlaying mafic lavas (Figs. 4 and 5). They appear as big patches of rust-colored Fe staining on the surface of the black volcanic rocks as a flocculent gelatinous deposit forming a thin continuous coating. At least five mineralized structures of hornitos-like chimneys were identified during the dive. Figures (Figs. 4A, B and 5A, D) show the general view and details of the hornitos chimneys where the samples of seawater (SV2/D16-N10, N14 and N16), biomineralized sediment, and bedrock were collected (SV2/D16-R9, R11, R12 and R15). The chimneys show variable sizes up to 5 m tall and 2–3 m wide, with columnar to conical morphologies. The hornito-like chimneys are composed by scoriaceous mafic lava spatter with a rough surface with numerous open conduits, which are surrounded by iron oxides ranging from whitish-yellow to rust colored, and covered by biomineralized sediment (Figs. 4C–F and 5A, 5C–D). The whitish yellow patches of oxides are abundant around active vent conduits at the base of the hornitos (Fig. 4C–D); and the reddish-brown patches appear on top of the hornitos around inactive vent orifices (Fig. 4F). The biomineralized sediment exhibits an intense red-orange color. They form an extensive mat covering all the substrate rocks on and around the chimney sites (Fig. 5B). Occasionally, whitish material with a flocculent filamentous texture appears surrounding the vent conduits on the external surface of the chimneys (Fig. 4E).

Table 2 shows the physico-chemical parameters (temperature, salinity, dissolved oxygen, depth) measured during the dive, as well as pH, ORP, and total Fe obtained from water sampled by ROV Niskin bottles. At a depth of 118 m (SV2/D16N10), the area affected by hydrothermal venting showed a seawater pH of 7.95, ORP 198 mV, and salinity 36.62 ‰ NaCl. The areas closer to the summit of the volcano (97–89 m water depth) showed higher pH (8.07–8.09) and salinity (36.70–36.84 ‰ NaCl) and lower ORP values (ca. 175) than at 118 m. Seawater samples had Fe and Mn contents ranging between 0.31 and 0.57 µM, and 0.01 and 0.24 µM respectively. The highest concentrations of Fe and Mn were measured in sample SV2/D16-N10, which was collected over vent conduits at the base of the hornito-like chimney (SV2/D16-R9) (Figs. 3D and 4C). In this area, concentrations of dissolved CO_2 were up to 568 µatm over the hornito structures, being one of the highest concentrations measured during the dive. During the dive, the measured temperature range was from 13.82 °C at 344 m water depth at the base of Tagoro volcano, to 18.73 °C at 89 m water depth at the summit. Between 89 and 120 m, the background mean temperature was 17.61 °C, with minimum values as low as 17.05 °C. Depth profiles of temperature (T) and dissolved CO_2 are shown in Fig. 6. Shimmering water was not observed at the hornitos or vent conduits, but slight thermal anomalies and CO_2 discharge within the area were detected during the dive, especially at the base of the hornitos, indicating diffuse-flow hydrothermal fluids and degasification of Tagoro volcano (Fig. 6).

The mineralized samples are representative of the areas of fluid venting. Sample SV2/D16-R9 was collected from a hornito-like chimney with columnar morphology (2 m wide and 5 m tall) located at 118 m water depth close to the summit of the volcano (Fig. 3D). Samples SV2/D16-R11 and SV2/D16-R12 were collected from another vent in a conical structure 3 m wide at the base and 2 m tall located at 115 m water depth and approximately 100 m west of the of sample SV2/D16-R9 (Fig. 3E). This area showed strong anomalies that included an

Table 2
Seawater physico-chemical parameters (pH, ORP, Fe and Mn concentrations, salinity, temperature, dissolved oxygen and CO_2, and depth) measured during the ROV dive.

Sample ID	pH	ORP (mV)	Fe (µM)	Mn (µM)	Salinity (‰ NaCl)	T (°C)	DO (% Sat.)	DO (mg/L)	CO_2 (µatm)	Water depth (m)
SV2/D16-R1	–	–	–	–	35.99	13.830	77.14	6.37	410	346
SV2/D16-N2	7.84	205	0.116	0.009	36.13	14.222	76.88	6.29	411	338
SV2/D16-R5	–	–	–	–	36.24	15.443	86.44	6.89	400	213
SV2/D16-C6	–	–	–	–	36.36	15.656	87.28	6.93	398	205
SV2/D16-R9	–	–	–	–	36.60	17.154	97.11	7.47	568	118
SV2/D16-N10	7.95	198	0.281	0.244	36.62	17.386	95.31	7.30	568	118
SV2/D16-R11 & R12	–	–	–	–	36.67	17.370	96.40	7.38	508	115
SV2/D16-N14	8.07	174	0.076	0.088	36.84	17.977	103.25	7.81	568	97
SV2/D16-R15	–	–	–	–	36.72	17.722	98.83	7.52	425	90
SV2/D16-N16	8.09	175	0.074	0.100	36.70	17.829	101.58	7.71	423	90

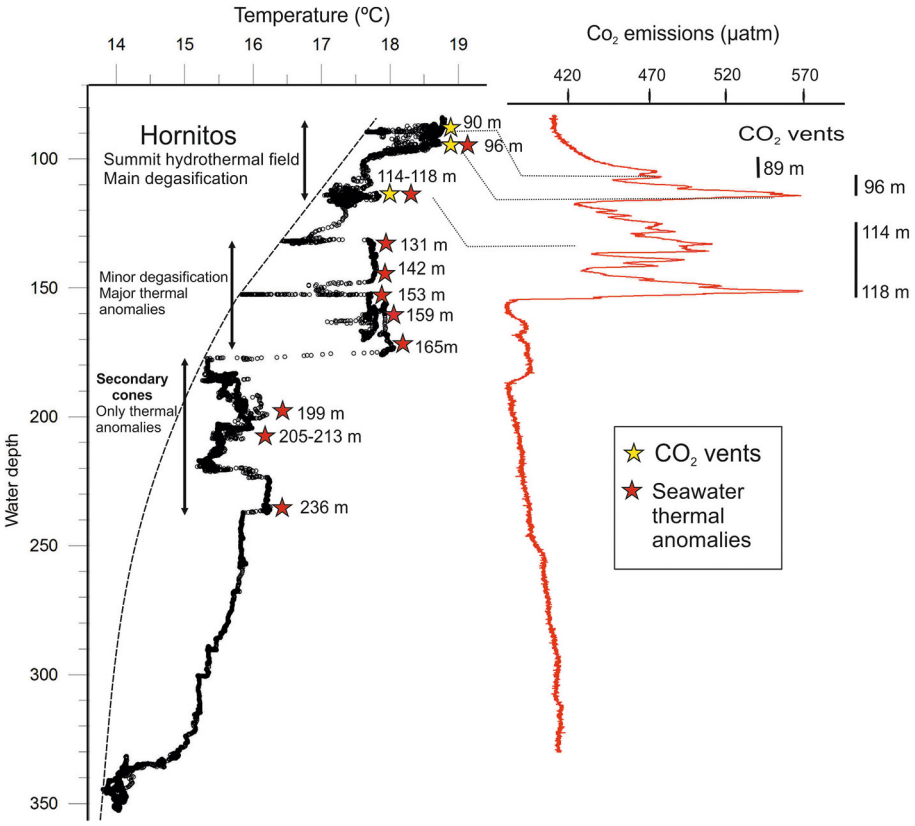

Fig. 6. Changes in temperature and CO_2 emissions with water depth as measured on ROV-Dive 16.

increase in T (range 17.38 to 17.58 °C), fluorescence (range 1.06 to 7.49 µg/L; base value 0.01 µg/L), and CO_2 (up to 508 µatm) together with a slight decrease of DO (range 7.54 to 7.37 mg/L). Other strong anomalies showed the same tendency in these parameters at 96 m, very close to where SV2/D16-N14 was sampled (e.g. T up to 18.24 °C and CO_2 568 µatm). Sample SV2/D16-R15 was collected from a fissure in volcanic rocks with a positive anomaly in CO_2 (425 µatm) located at 90 m water depth at the top of the volcano but lower than in the station SV2/D16-N14 (Fig. 3F and Table 2). Samples SV2/D16-R9, SV2/D16-R11, and SV2/D16-R12 are mafic lavas covered by orange 5 mm-thick unconsolidated sediment rich in Fe oxyhydroxides and silica. Sample SV2/D16-R15 is a submillimeter patina of Fe oxyhydroxides covering bedrock. The samples were soft and spongy-gelatinous immediately after recovery. The biomineralized sediment was not lithified and the water column was tainted by oxyhydroxides during the recovery operations.

4.1.2. Secondary cones hydrothermal field

Submersible survey SV2/D16 showed another area affected by hydrothermal venting in the region of the fissure-hosted secondary cones (213–185 m water depth) defined by Somoza et al. (2017) (Fig. 7). The area is composed of bright reddish-orange to yellow Fe oxyhydroxides forming laminated sequences of soft friable deposits on top of lava blocks and cementing brecciated lavas and scoria-lapilli deposits (Figs. 7A-C). In addition, areas within this secondary-cones site showed a discontinuous whitish-yellow color probably formed by mixing of oxyhydroxides and silicates (i.e., ferrihydrite, volcanoclastic material) (Fig. 7D).

Samples SV2/D16-R5 and SV2/D16-C6 were collected from an area covered by scoria and lava blocks with hydrothermal manifestations (Fe-oxyhydroxide precipitates and seawater physico-chemical perturbations (mainly less salinity and some increase in T, but not in CO_2 or fluorescence), located at 213 and 205 m water depth, respectively (Fig. 3B and C). The first hydrothermal discharge manifestations appeared at 236 m water depth where the temperature was 16.24 °C, but no hydrothermal mineralization during the dive was observed. Between 215–185 m, the mean temperature was 15.62 °C (± 0.27 °C), but a thermal anomaly was registered at 199 m water depth with values of up to 16.20 °C. Sample SV2/D16-R5 is a fragment of scoriaceous black volcanic rock covered by an unconsolidated yellowish-orange patina rich in Fe oxyhydroxide and silica.

(Figs. 3B and 7A). Sample SV2/D16-C6 is composed by multiple millimeter to centimeter fragments of black scoria covered by an orange patina rich in Fe oxyhydroxide (Figs. 3C and 7C). The intermediate area between the secondary cones and the summit of the principal cone (165–131 m water depth) is steep (25–35°) and formed by abundant black scoria with dispersed angular blocks of a centimeter to decimeter in size and covered by orange Fe oxyhydroxide. They might have been ejected as lithics from previous edifices formed at the summit through explosive eruptions as proposed by Somoza et al. (2017). Nevertheless, positive thermal anomalies have been detected in this area (range 16.87 and 17.81 °C), together with negative salinity anomalies (range 36.59–36.75 ‰ NaCl).

4.2. Textural features and mineralogy

The mineralogy and geochemistry of the mineralized samples collected from the two areas of hydrothermal activity, the summit and mid-southeast flank of Tagoro volcano, exhibit similar characteristics. The following sections describe the textural features, mineralogy, and chemistry.

4.2.1. Fe-oxyhydroxide mineralization

The mineralized samples represent the uppermost 5 mm of colloidal-like material that covers the volcanic bedrock (black mafic rocks). Some distinctive characteristics exist among the samples

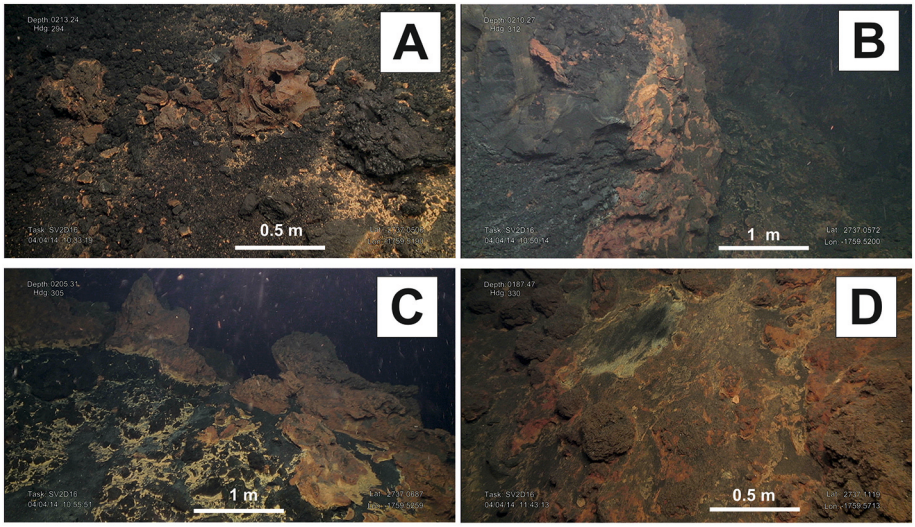

Fig. 7. ROV images of the secondary cones hydrothermal field along the SE flank of the Tagoro volcano. A) Scoriaceous brownish lava blocks with large vesicles and orange Fe-oxyhydroxide mineralization (213 mwd). B) Reddish-orange Fe oxyhydroxide cemented brecciated lavas. C and D) Ponds of hydrothermally altered seafloor with lapilli deposits (black) and hydrothermal sediments (yellow-orange) surrounded by scattered scoriaceous lava blocks stained by oxyhydroxides. (For interpretation of the references to colour in this figure legend, the reader is referred to the web version of this article.)

collected at the two hydrothermal fields defined in the previous section. These samples are composed mainly of low-crystalline to amorphous Fe oxyhydroxides (proto-ferrihydrite, ferrihydrite). The XRD broad reflections or no reflections attest to the amorphous nature and nanometer-scale crystallite size of the mineralization (Fig. 2S). Samples SV2/D16-R5ox, SV2/D16-C6ox and SV2/D16-R12ox have no distinct peaks except for one broad hump at approximately 35° (2 T). This hump may be groups of adjacent diffuse reflections, and indicate the presence of hydrous iron oxide (proto-ferrihydrite and ferrihydrite) with reflections at 2.5 and 1.5 Å. Sample SV2/D16R15ox shows the abundance of gypsum showing principal peak reflections at 7.63 (100), 4.283 (100) and 3.065 Å (75), in addition to nearly amorphous oxyhydroxides (Fig. 2S). Small volcaniclastic ash particles (clinopyroxene) were detected by XRD and confirmed under the microscope in the mineralized sample SV2/D16-R9ox (Fig. 2S), although most of the ash would be amorphous volcanic glass shards.

The Fe-oxyhydroxide deposits show under the petrographic and electron microscopes a micro-dentritic, branching-columnar stromatolitic texture (frutexite-like) (Fig. 8A–B), composed essentially of Fe oxyhydroxides. In thin section each column is characterized by a reddish-black color specific to Fe oxyhydroxides. The branching columns provide for high porosity, which results from the open space between the columns. Frequently, scattered micrometric crystal aggregates of pyrite (1–7 μm) are observed at the base of these stromatolite-like structures in contact with the mafic substrate (Fig. 8A–B).

SEM photomicrographs of these Fe-oxyhydroxide sediments show the most characteristic textural features of mineral constituents (Fig. 9). The Fe oxyhydroxides display a general porous sugary texture, frequently forming botryoidal aggregates and covering microbial cells (Fig. 9A) (see section 4.4 Geo-microbiology). Abundant euhedral tabular, prismatic and acicular microcrystals of gypsum (up to 80 μm long) can be observed in all the mineralized samples. They frequently appear as clusters of crystals with striated and warped surfaces, mixed with and covered by Fe oxyhydroxides (Fig. 9B). Octahedral microcrystals and framboids of pyrite, isolated or forming clusters, are in contact with the substrate volcanic rock and occur at the base of Fe-oxyhydroxide mineralization (Fig. 9C). The pyrite is pseudomorphed by the Fe oxyhydroxides. Aggregates of blade-like crystals of Mn oxides occur in sample SV2/D16-R15ox (Fig. 9D). Opal appears as a coating of microbial cells forming a closely packed globular texture with an overall botryoidal appearance (see section 4.4 Geo-microbiology). Opal is especially abundant in the sample SV2/D16-R15ox (Fig. 9E). Crystal aggregates forming lepispheres of silicates (zeolites?) occur in sample SV2/D16-R12ox (Fig. 9F). Electron microprobe analysis of oxyhydroxides are given in Table 2S.

4.2.2. Mineralized bedrock

The volcanic bedrock is black with a moderate to highly vesicular texture (25–40 vol% vesicles). Variations in vesicle size from millimetre to centimeter scale give rise to a banded structure. The rock is relatively crystal rich, with 5-20 vol% phenocrysts of forsteritic olivine, Ti-rich diopside and euhedral titanomagnetite. The groundmass ranges from glassy to cryptocrystalline, the latter being composed of olivine, clinopyroxene and titanomagnetite microlites as well as scarce, needle-like Ca plagioclase (Fig. 8). More detailed information on the mineralogy and petrography of host rocks can be found in Somoza et al. (2017). Pyrite occurs as small particles filling degasification vesicles and microcracks as well as forming veinlets and veins crosscutting titanomagnetite, olivine, clinopyroxene, and volcanic glass (Figs. 8C, D). The pyrite-rich micro veins are abundant in all bedrock samples and show a cracking pattern with a submillimeter width and millimeter to centimeter length. Occasionally pyrite in the veins is slightly altered to Fe oxyhydroxides. Minor to rare chalcopyrite occurs as microcrystals (1–5 μm) dispersed in the volcanic bedrock or filling degasification vesicles. Anhydrite-gypsum minute idiomorphic crystals (< 5 μm) are also found filling-in and surrounding vesicles (Figs. 8E, F). Titanomagnetite is the most widespread opaque mineral in the bedrock, where it is especially abundant in the groundmass occurring as numerous, very small (< 1–5 μm) skeletal crystals indicating rapid quenching of the basalt. Magnetite phenocrysts are rare and occur in small subhedral grains up to 100 μm or as inclusions in silicate phenocrysts. Some titanomagnetites in the bedrock show hematite replacement along grain boundaries and fine pyrite veinlets crosscutting the crystals, the groundmass, and silicate phenocrysts (Fig. 8D). The microscopic observations suggest crystallization of magnetite from a basalt melt simultaneously with the formation of silicate phenocrysts and ending with rapid cooling and formation of the glassy groundmass.

4.2.3. Non-mineralized mafic lavas and sediments

The non-mineralized volcanic bedrock SV2/D16-R1 collected at the base of the volcanic edifice at 346 m water depth (Fig. 1–3), an area without evidence of hydrothermal activity, is black with a highly vesicular texture (50 vol%) with essentially the same textural features and mineral composition as the mineralized bedrock. Nevertheless, pyrite, chalcopyrite, and gypsum-anhydrite are absent in these bedrock samples and cracking patterns with sulfide veinlets are also not observed.

Offshore the western part of El Hierro Island, core SV1/TG16 penetrated 2.87 m below seafloor (Fig. 3S). It is composed of two main sedimentary sections differentiated on the basis of textural features, microfossils, color, major, minor and trace element geochemistry, and mineralogy. The upper section (0–2.48 m) is dominated by brown to

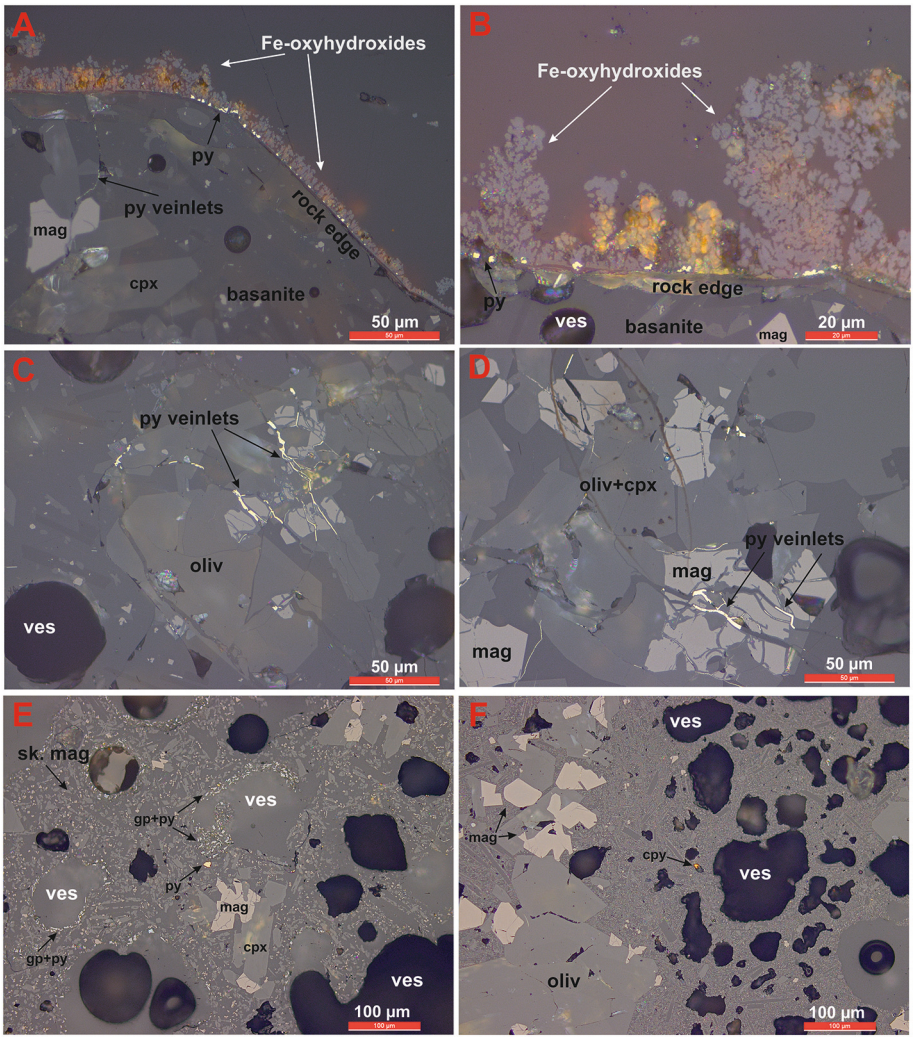

Fig. 8. Thin and polished-section photomicrographs of Fe-oxyhydroxide mineralization of sample SV2/D16-R12ox. A and B) dendritic, branched columnar stromatolitic micro-texture (frutexite-like) formed by Fe oxyhydroxides overlaying basanite with olivine (oliv), clinopyroxene (cpx), and magnetite (mag). Minute pyrite crystals (py) mark the mineralization substrate surface contact. C and D) pyrite veinlets crosscutting bedrock minerals. E and F) Pyrite, chalcopyrite (cpy), and gypsum (gp) filling vesicles (ves) in basanite substrate with abundant skeletal magnetite (sk. mag).

ochre hemipelagic biogenic calcareous mud rich in foraminifera and coccolith tests. The lower section (2.48–2.87 m) is dominated by grey-olive siliciclastic mud dominated by phyllosilicates (smectite ± kaolinite ± palygorskite) and quartz, with lesser K-feldspar, plagioclase, and calcite. This core contains other traces of volcanogenic minerals and their alteration products (forsteritic olivine, clinopyroxene, amphibole, phyllosilicates). There is no evidence of Fe-oxyhydroxide precipitation or Fe-smectites associated with hydrothermal fluids along the core section.

4.3. Chemical composition

4.3.1. Fe-oxyhydroxide mineralization

The Fe-oxyhydroxide deposits show a variable chemical composition (Table 3), with high contents in Fe_2O_3 (28–58 wt% = 31–65 wt% FeOOH) and moderate SiO_2 (up to 11.3 wt%) and P_2O_5 (1.4–5.1 wt%). Silica is highly enriched relative to alumina in the mineralized samples (SiO_2/Al_2O_3 up to 103) and compared to the mafic volcanic bedrocks and effusive non-mineralized lavas (SiO_2/Al_2O_3 = 3.2–3.3), and non-mineralized sediments from offshore west of El Hierro Island (SiO_2/Al_2O_3 = 3–8). The Fe_2O_3/Al_2O_3 ratios of the mineralized samples are up to 531 compared to a mean of 1.1 for volcanic rocks and 0.31 for the non-mineralized core sediments. The relatively elevated contents of Al, Ca, Mg and Ti in sample SV2/D16-R9ox are in good agreement with the observation that this sample contains minor pyroxene (see XRD observations). Mn and Fe are highly fractionated, (Fe/Mn > 700) and combined Co, Ni, and Cu contents are very low in the iron-mineralized samples. These deposits plot in the lower left corner on the ternary diagram of Bonatti et al. (1972) (Fig. 12, blue spots) indicating a hydrothermal origin. With respect to trace elements, they are variable in the four mineralized samples analysed (Table 3). Sample SV2/D16-R9ox is the most enriched in metals especially the contents of V (737 µg/g), Cu (584 µg/g), Sr (334 µg/g), As (318 µg/g), Ba (147 µg/g), and Ni (102 µg/g). Other elements like Zn, Mo, Co, or U are abundant in the mineralized samples. Concentrations of As, Co, Cu, Mo, Ni, U, V, and Zn are enriched relative to those in non-mineralized sediment samples from the west of El Hierro Island. As, Co, Cu, Mo, Pb, U, V, and W concentrations are enriched in the mineralized samples compared to the volcanic bedrock. The total REY contents are markedly low for samples SV2/D16-R12ox (15 µg/g) and SV2/D16-R11ox (57 µg/g); and low for sample SV2/D16-R9ox (286 µg/g). The low REY concentrations in the mineralized samples (15–57 µg/g) contrast with those of the non-mineralized control core samples of 98 and 128 µg/g. Chondrite-normalized REY patterns show the high fractionation between the light and heavy REY (Fig. 10A); sample SV2/D16-R9ox is strongly LREE enriched and samples SV2/D16-R11ox and SV2/D16-R12ox are less enriched in

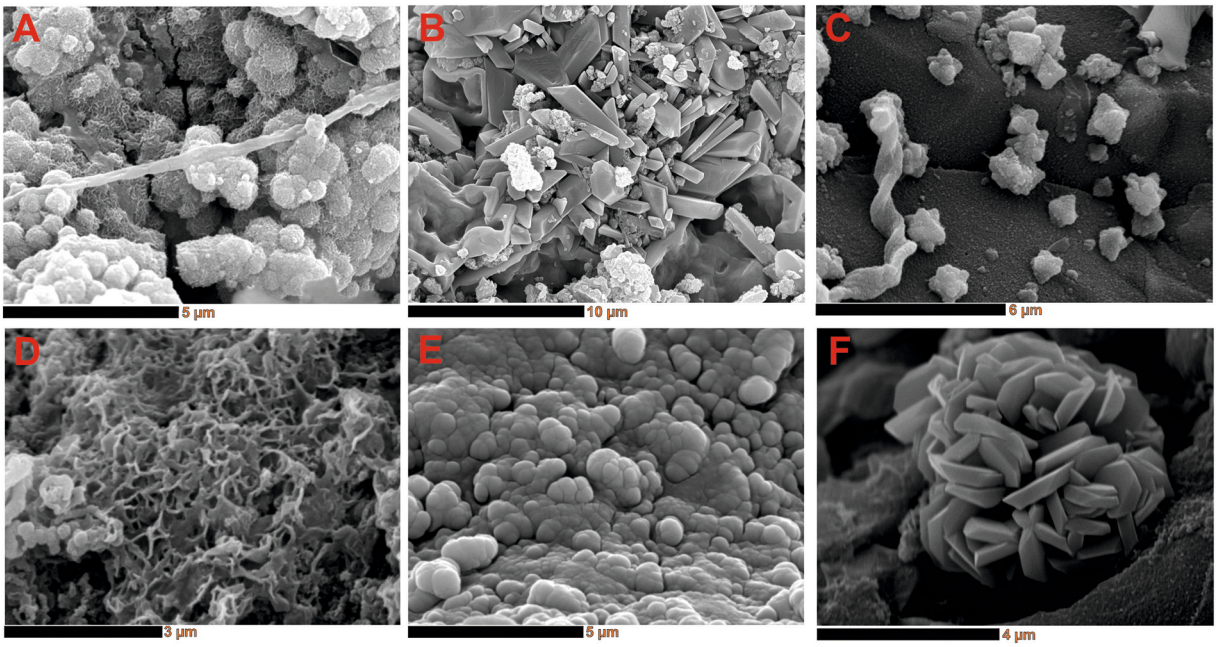

Fig. 9. SEM photomicrographs of Fe-(Mn) oxyhydroxides and opal-A mineralization. A) Micro-botryoidal to spheroidal Fe minerals, sample SV2/D16-R9ox. B) Euhedral tabular and prismatic microcrystals of gypsum partially covered by Fe oxyhydroxides, sample SV2/D16-R9ox. C) Fe-oxyhydroxides pseudomorphs after pyrite octahedral microcrystals at the base of mineralization in contact with the substrate volcanic rock, sample SV2/D16-R12ox. D) Webbed complex of Mn oxides, sample SV2/D16-R15ox. E) Opal-A forming a closely packed globular texture with an overall botryoidal appearance, sample SV2/D16-R15ox. F) Lepisphere of silicates (zeolites?) in a vesicle filling, sample SV2/D16R12ox.

LREY. Eu anomalies are slightly positive (0.92–0.94), and no anomaly to slightly negative Ce anomalies characterize the mineralized samples. The non-mineralized control core samples are enriched in LREE and show slightly positive Eu anomalies (0.99–1) and small negative Ce anomalies (−0.03). Shale-normalized REE patterns show the most striking features for these mineralized samples: little fractionation between the light and heavy REEs (Fig. 10B). Eu anomalies are strongly positive (1.41–1.47) for the three Fe-mineralized samples shown in Fig. 10B. Ce shows a very slightly negative anomaly for sample SV2/D16-R9ox, positive anomaly for sample SV2/D16-R11ox, and probably analytical issues with the sample SV2/D16-R12ox as concentrations are very low. The non-mineralized control core samples are slightly enriched in HREE and show no to very small Eu anomalies.

The microprobe analyses listed on Tables 2S and 3S reflect point analysis on microscopic oxyhydroxide layers and pyrite micro-crystals located at the base of oxyhydroxide layer in sample SV2/D16-R12ox. The oxyhydroxide dendritic columns show enrichments with respect to the bulk average composition in Fe (46.7 wt %), Si (up to 8.4 wt %), and P (up to 2.8 wt %) and less enrichment in Mg (up to 1.8 wt %) and Ca (up to 0.7 wt %). Pyrite micro-crystals, frequently affected by oxidation after collection, show enrichments in Bi (up to 1400 µg/g) and Co (up to 1100 µg/g) and lesser enrichment in Ni (up to 400 µg/g).

4.3.2. Mineralized bedrock

Chemical analysis of three mineralized bedrock samples shows their alkaline basaltic composition (Table 3) classified as basanite based on the total alkalis silica diagram of Le Maitre et al. (1989): low silica (41.5–41.9 wt %) and relatively high MgO (7.5–7.8 wt %), together with Ni (120–154 µg/g) and Co (48–59 µg/g) contents are close to unaltered basalt composition. The microprobe analyses of sulfides (pyrite, chalcopyrite) and native copper filling cracks or vesicles and the dispersed magnetite (enriched in Ti, Al, Mg) in basanite sample SV2/D16-R12 are listed in Tables 3S and 4S. Pyrite veinlets and vesicle fillings, showing a variable degree of oxidation, display similar chemical composition to those in the Fe-oxyhydroxide mats. They are enriched in Co (up to 2100 µg/g), Ni (up to 2600 µg/g), and Bi (up to 1700 µg/g). Minute dispersed grains of chalcopyrite and Cu-rich pyrite show enrichments in Ni (up to 3.3 wt %) and Co (up to 2700 µg/g). Skeletal-shaped magnetite shows enrichments in Ti (up to 14.7 wt %) and Mg (up to 4.3 wt %). Non-skeletal magnetite included in silicates frequently is enriched in Cr (up to 4.2 wt %).

4.3.3. Non-mineralized basanite and sediment

Samples taken from the non-mineralized basanite lava showed a similar chemical composition (Table 3). Cu and W exhibit a slight enrichment in the mineralized bedrock (up to 114 and 11 µg/g respectively) compared to the non-mineralized volcanic rock (89 and < 2.2 µg/g respectively).

Mud samples collected from sediment core SV1/TG16, show two geochemical types: carbonate- and silicate-dominated sections (Table 5S). The upper section of the core (05 cm) contains high CaO (40 wt %) and lesser SiO_2 (14 wt %) and Al_2O_3 (5 wt %). The lower section of the core (248-255 cm) contains high SiO_2 (59 wt %) and Al_2O_3 (8 wt %) and lower CaO (12 wt %). In addition, high TOC and LOI in the upper core section, 3 wt % and 36 wt % respectively, are much less in the lower core section, 0.1 wt % and 13 wt % respectively. Both core sections show variations in silicate and carbonate components for major and trace elements concentrations normalized to a typical average shale (Turekian and Wedepohl, 1961; Baturin, 1988).

4.4. Iron isotopes

Iron Isotope data were acquired for two samples representative of the Fe-oxyhydroxide sediments removed from the surface of sample SV2/D16-R12ox, as well as from the top layer of a Fe-Mn crust (DRAGO0511/DR16-14) from Tropic Seamount (SW of El Hierro Island). The δ^{56}Fe and δ^{57}Fe values for the Fe-oxyhydroxide mineralized samples are respectively +0.383 (± 0.015) ‰ and + 0.570 (± 0.045) ‰. The values obtained for the Fe-Mn crust are δ^{56}Fe -0.46 (± 0.07) and δ^{57}Fe -0.64 (± 0.14), both relative to the standard IRMM-014.

Table 3
Bulk chemical composition of mineralized samples and volcanic bedrock.

(Expedition SUBVENT 2, Dive D16) Oxides, bedrock and non-mineralized rocks								
	D16-R09ox	D16-R11ox	D16-R12ox	D16-R15ox	D16-R9[a]	D16-R12[a]	D16-R15[a]	D16-R01[a]
	Fe-oxyhydroxides mineralized samples				Basanite bedrock			Non-mineralized basanite
Al_2O_3 (wt.%)	5.57	0.68	0.11	2.63	12.6	12.7	12.9	12.6
SiO_2	–	–	11.3	–	41.5	41.9	41.9	41.4
P_2O_5	1.63	5.13	4.82	1.4	0.77	0.78	0.78	0.77
K_2O	0.39	0.11	0.06	0.31	1.38	1.38	1.41	1.38
Na_2O	1.34	1.09	0.3	8.16	3.59	3.42	3.69	3.76
CaO	3.32	0.65	1.75	3.03	10.3	10.4	10.4	10.2
MgO	1.99	0.49	0.71	2.79	7.82	7.79	7.48	7.91
TiO_2	2.6	0.18	< 0.3	0.88	4.64	4.63	4.68	4.61
Fe_2O_3	41	52.2	58.4	27.6	14.6	14.4	14.5	14.6
FeOOH	46.1	58.6	65.6	31				
MnO	0.35	0.13	0.07	3.4	0.18	0.17	0.17	0.18
TOC	–	–	0.14	–	< 0.01	0.12	0.02	0.02
S	–	–	0.04	–	0.06	0.1	0.05	0.06
LOI	—	–	23.5	–	0.61	−0.12	−0.21	0.27
SiO_2/ Al_2O_3	–	–	103	–	3.3	3.3	3.2	3.3
Ag (μg/g)	0.4	0.1	3	2	0.2	–	0.2	0.1
As	318	23	25	250	4	< 3	3	3
Ba	147	104	83	128	349	407	351	343
Be	1	0.2	< 0.1	0.5	2	–	2	–
Co	88	98	1	22	53	59	48	55
Cr	96	21	17	31	222	223	190	207
Cu	584	170	3	318	88	114	101	89
Hg	–	–	–	–	0.01	0.03	0.02	0.01
Li	< 17	< 17	< 17	< 17	< 17	< 17	< 17	–
Mo	67	12	13	40	4	3	4	3
Nb	36	< 10	–	21	75	75	77	74
Ni	102	126	4	12	154	140	120	141
Pb	10	< 2	3	12	6	3	4	3
Rb	< 20	< 20	< 20	32	32	32	33	32
Sb	2	0.4	2	2	< 2	< 2	< 2	< 2
Sc	9	1	< 1	2	35	22	35	34
Se	12	2	2	< 5	9	–	9	9
Sr	334	188	522	464	868	876	882	863
Th	3.05	0.24	0.44	1.05	< 1.5	8.6	10.8	6.7
Tl	< 0.1	1	< 0.1	< 0.1	< 1.6	< 1.6	< 1.6	< 1.6
U	9.85	1.94	1.73	1.9	< 1	< 1	< 1	< 1
V	737	43	34	552	364	388	364	351
W	56	32	43	200	< 2.21	11	11	< 2.21
Zn	76	38	11	94	125	135	125	121
La	47.3	9.51	3.11	–	51.3	50.2	54.2	53
Ce	103	23.5	4.87	–	110	107	117	113
Pr	13	2.12	0.48	–	14	13.9	14.8	14.4
Nd	54	8.55	2.04	–	58.7	59.7	61.9	60.7
Sm	10.8	1.72	0.46	–	12.6	12.2	12.9	12.6
Eu	3.22	0.53	0.14	–	3.84	3.77	4.15	4.02
Gd	9.7	1.73	0.46	–	11	10.6	11.7	11.3
Tb	1.27	0.24	0.05	–	1.49	1.42	1.57	1.46
Dy	6.73	1.23	0.4	–	7.5	7.25	7.87	7.48
Y	30	6.17	2.49	–	30.1	29.6	31.1	30.5
Ho	1.19	0.23	0.08	–	1.25	1.21	1.35	1.29
Er	3.04	0.62	0.23	–	3.09	2.98	3.24	3.1
Tm	0.4	0.08	0.03	–	0.37	0.36	0.39	0.38
Yb	2.35	0.43	0.17	–	2.23	2.08	2.3	2.2
Lu	0.34	0.08	0.03	–	0.32	0.28	0.32	0.29
ΣREY	286.3	56.74	15.04	–	307.79	302.55	324.79	315.72
Ce[a]	−2.59	0.09	−0.07	–	–	–	–	–
Eu[a]	1.35	1.31	1.3	–	–	–	–	–
Ce_{SN}/Ce_{SN*}	3.42	4.04	2.71	–	–	–	–	–
Y_{SN}/Ho_{SN}	25.21	26.83	31.13	–	–	–	–	–

Fe-oxide mineralized samples: major elements determined by ICP-AES except the sample R12 analyzed by XRF; trace elements by ICP-MS except Li, Nb, Rb, Sc, Sr and W determined by ICP-AES.

[a] Bedrock and non-mineralized rocks: XRF results; Ag and Be determined by ICP-MS; Li determined by ICP-AES

4.5. Geomicrobiology

4.5.1. Mineralized microbial morphologies

Microbial-related structures were observed under the SEM within the mineralized samples (Figs. 11 and 6S). Different morphotypes are distinguished: twisted stalks (Fig. 11A–C), empty straight sheaths (Fig. 11D), rod-shaped microorganisms (Fig. 11C and E) and filamentous bodies (Fig. 11F). They are widely scattered throughout all the samples, the twisted stalks being the most abundant. Twisted stalks and straight sheaths are formed by bacteriogenic Fe-oxyhydroxide

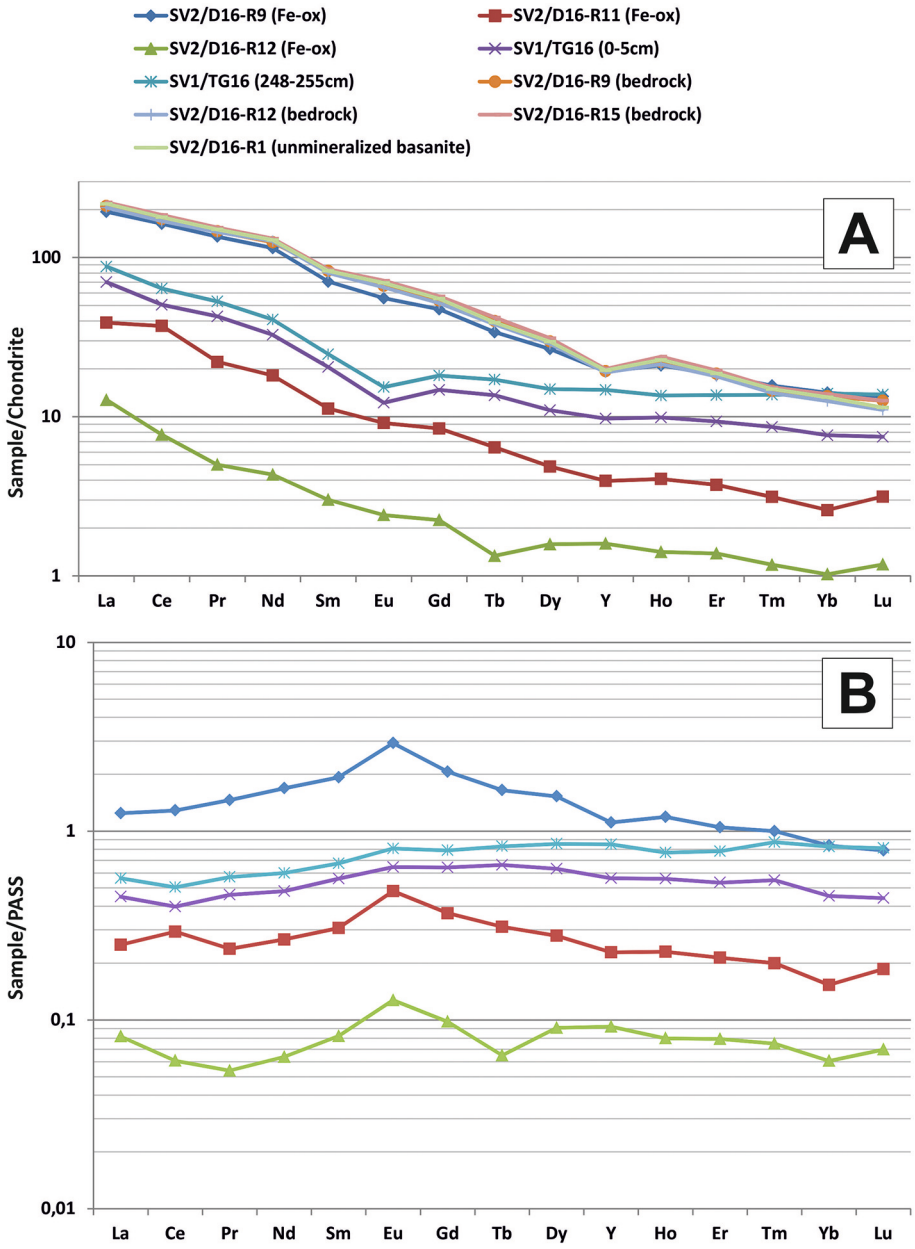

Fig. 10. A) Chondrite-normalized REY plots for mineralization samples, sediment, and un-mineralized basanite. B) PAAS-normalized REEs plots for this group of studied samples; Chondrite from Palme et al. (1981); PAAS from Taylor and McLennan (1985).

precipitates forming floccule of microbotryoidal texture, which gives it an orange-brown color. Stalks and sheaths are > 10 μm long with a diameter of 1–2 μm. Twisted stalks formed by unique mineralized fibrils are compacted and tangle up with other stalks and precipitates. Twisted stalks are most abundant in the summit vent samples (i.e. D16-R9, D16-R12ox and D16-R15ox), but also form dense mats represented by sample SV2/D16-R5ox from the secondary vents (Fig. 11A).

Straight sheaths are generally scattered and not as abundant.

Rod-shaped microorganisms 1–2 μm long are found covered by opal-A in sample SV2/D16-R15ox (Fig. 11E), and covered by bacteriogenic Fe-oxyhydroxide precipitates above volcanic substrates in sample SV2/D16-R9ox. Filamentous bodies are detected in sample SV2/D16-R15ox with bodies up to 5 μm long and covered by opal-A and thus the bodies are hardly distinguishable from the surface (Fig. 11F). Mineralization of these microbial-related structures enlarges or modifies their original dimensions.

4.5.2. *Bacterial and archaeal 16 s rDNA sequences from an active vent*

Environmental DNA analysis performed on sample SV2/D16-R12ox revealed that the majority of the ubiquitous bacterial and archaeal taxa are ones commonly found in the water column (Fig. 5S). Around 50% of the bacterial DNA relative abundance is related to *Marinomonas* sp., while *Candidatus* Nitrosopumilus sp. represents up to 85% of the archaeal DNA relative abundance. Other taxa that also thrive in these environments were detected, e.g. Acidobacteria, Bacteroidetes, *Pseudoalteromonas* sp., Thermoplasmata, Woesearchaeota (DHVEG-6) and *Candidatus* Nitrosopelagicus (Walsh et al., 2016; Bergauer et al., 2018). Sulfur-oxidizing bacteria constitute most of the remaining bacterial community (up to 19%), represented mainly by Gammaproteobacteria from the orders Thiotrichales and Chromatiales (Ectothiorhodospiraceae and *Thiohalophilus* sp.). Sulfate-reducers from the genus *Desulfobulbus* (Deltaproteobacteria) represent 4.56% of the bacterial relative abundance (Fig. 5S). Only a few reads were clustered and related to unknown iron-oxidizing Zetaproteobacteria (0.44%) and iron-reducing

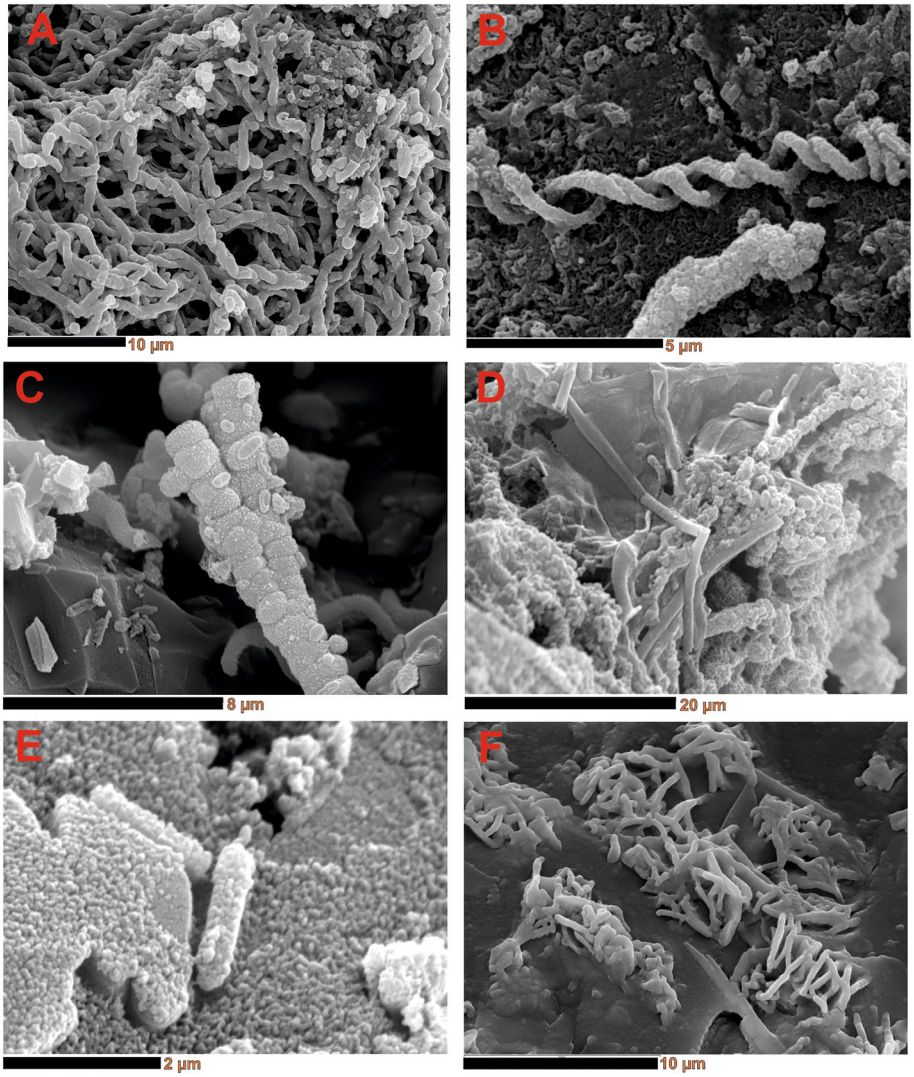

Fig. 11. SEM photomicrographs of microbial-related structures from Fe-oxyhydroxides mineralized mats on Tagoro volcano. A) Dense mat of twisted stalks, sample SV2/D16-R5ox. B) Twisted stalk from sample SV2/D16-R15ox; note sub-micrometer grains mineralizing the surfaces. C) Super-twisted stalks composed of stacked ca. 1 µm diameter cells; note twisted stalks in the background, sample SV2/D16-R12ox. D) Straight empty sheaths from sample SV2/D16-R9ox. E) ca. 2 µm long rod-shaped microorganisms coated by opal-A from sample SV2/D16-R12ox. F) Mass of filamentous branching bodies coated by opal-A from sample SV2/D16-R15ox.

Deferrisoma (0.04%) (Table 6S). Furthermore, methanogenic archaea, i.e. *Methanosarcina* sp. (2.62%) and *Methanoccoides* sp. (0.20%) were also present in the sample, as well as some reads are related to ANME archaea (0.21%) and GOM Arc I (0.03%), known to oxidize methane (Fig. 5S; Table 6S).

5. Discussion

5.1. Evidence of early hydrothermal activity after the volcanic eruption

From a hydro-chemical point of view, several lines of evidence of hydrothermal activity were noted, identifying two main areas: (i) a summit hydrothermal field and, (ii) secondary-cones hydrothermal field as described above.

Noticeable anomalies in carbon dioxide (between 423–568 µatm) were found in areas close to the summit of the volcano, in the hornitos (Table 2 and Fig. 6). These anomalies were already mentioned by Santana-Casiano et al. (2018). Furthermore, in that study, the areas with CO_2 emissions below 414 µatm were classified as *unaffected* by volcanic emissions. Similar background values were measured in our deep areas at the base of Tagoro volcano (Fig. 6).

The emission of CO_2 generates local water acidification affecting the chemical equilibrium and speciation and could impact biological communities, with especially important consequences for organisms that use calcium carbonate in their structures (e.g. scleractinian corals). Seawater sample SV2/D16-N10 from the summit of the volcano showed minor acidification, together with a high concentration of CO_2 (up to 568 µatm) and high fluorescence values (up 10 µg/L), which could be associated with the presence of methanogenic archaea (*Methanosarcina* sp., *Methanoccoides* sp., ANME).

Hydrothermal activity and Fe-oxyhydroxide sediment deposition are restricted to areas near the summit (Figs. 4 and 5) and in the secondary cones following a NW–SE trend along the southeastern flank (Fig. 7). In addition, according to T data, two other areas could support hydrothermal activity, one between 236–215 m and the other between 165–131 m water depths respectively, where a high number of positive anomalies were identified (Fig. 6).

The hydrothermal fluids are charged with Fe, Si, and Mn and minor amounts of other metals. This chemistry of expelled fluids is common in other hotspot hydrothermal vents (Michard et al., 1989; Puteanus et al., 1991; Hekinian, 2014) with diffuse-flow low-temperature (< 30–60 °C) hydrothermal fluids egressing from centimeter-scale orifices and forming thin slabs of Fe oxyhydroxides on the surrounding seabed. Fluids expelled from multiple shallow-water vent sites in the studied

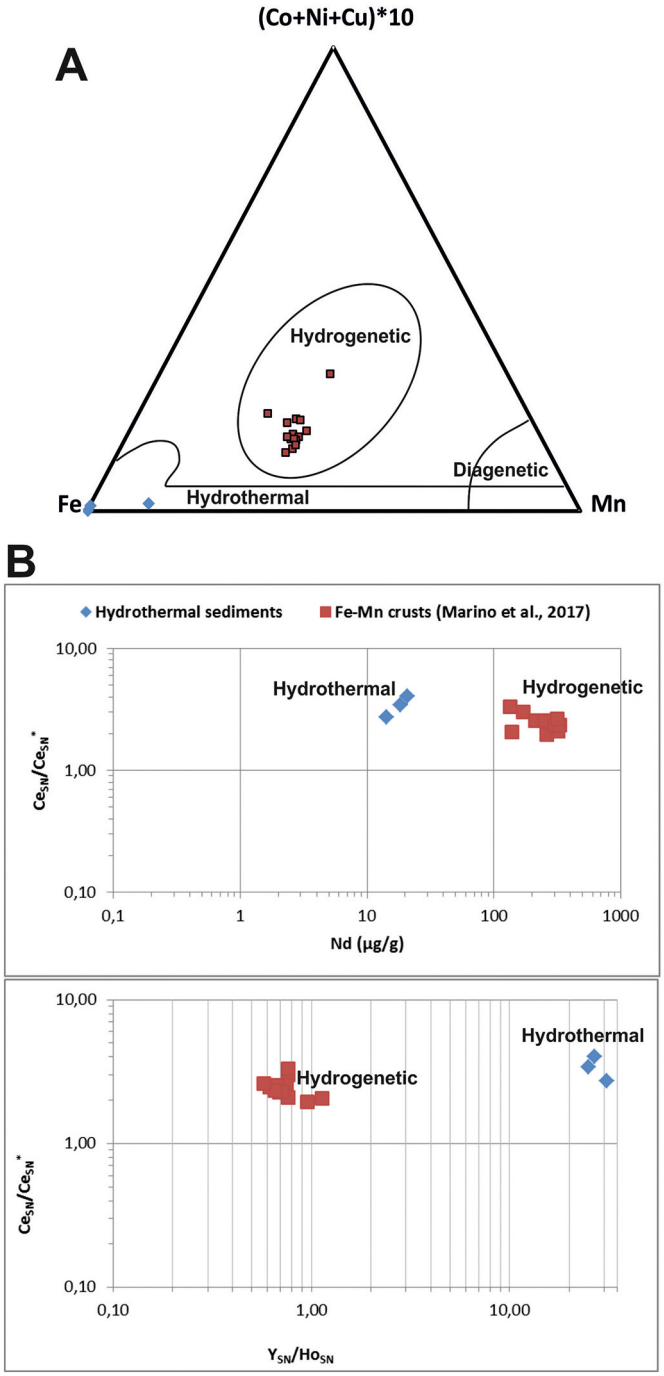

Fig. 12. A) Ternary plots for Tagoro mineralized samples in comparison with Canary Island Seamount Province Fe-Mn crusts (Marino et al., 2017), after Bonatti et al. (1972); the Fe-oxyhydroxide sediments plot in the hydrothermal field. B) Plot of Tagoro mineralized samples on graphs of Ce_{SN}/Ce_{SN} vs Nd concentration and Ce_{SN}/Ce_{SN} vs Y_{SN}/Ho_{SN} ratios (after Bau et al., 2014) in comparison with Fe-Mn crust deposits (Marino et al., 2017). The Tagoro mineralized samples plot in the hydrothermal field on these diagrams.

area revealed temperatures around 38–40 °C, while the ambient seawater temperature was 18–20 °C (Hannington et al., 2016). Fe is of particular interest because it is almost quantitatively precipitated from solution in buoyant and non-buoyant plumes (Fig. 2). After the hydrothermal emission, Fe(II) is oxidized in the presence of DO and precipitates as various mineral forms; around 4% of the total emitted iron is stabilized against loss from solution due to complexation by dissolved organic ligands or by incorporation into inorganic or organic colloids (Resing et al., 2015). The seawater samples showed high concentrations of dissolved Fe, especially sample SV2/D16-N10 (Fe 0.281 µM, Table 2). Concentrations at the surface of the ocean are typically < 0.3 nM, and range between ca. 0.2–1.2 nM in the deep ocean (> 1000 m) (De Baar and De Jong, 2001; Hunter and Boyd, 2007). On the other hand, during the period of volcanic activity, the emissions generated reduced Fe species reaching very high values (50 µmol kg^{-1}, Santana-Casiano et al., 2013). The interaction of ferrous iron with organic compounds slows down the rate of iron precipitation and formation of Fe hydroxides (Theis and Singer, 1974; Gledhill and Buck, 2012). The organic complexation drives the solubility of Fe and some other trace metals and promotes the precipitation of oxyhydroxides far away from the vent sites. After the eruption, columns consisting of streams of gas bubbles emerging directly through the sandy to pebbly unconsolidated pyroclastic deposits and through fractures in volcanic rocks were seen along the ROV track taken from IGN (IGN, 2012), which was interpreted to be diffuse discharge of fluids.

The mineralized deposits are distributed in and around the hornitos (Fig. 13). The lateral distribution of mineralization must be related to the hydrothermal plume, which after egress from the hornito vents is displaced laterally by bottom currents promoting a potentially wider distribution of Fe-oxyhydroxide encrustations at the summit of the underwater volcano. The different shapes of the plumes reflect the distinct nature of the flares (Fig. 2A). The occurrence of particulate material might generate a denser plume that would reach the level neutral buoyancy at deeper depths than those formed uniquely by gas. At a certain depth level, if ascending bubbles of gas that drive the upward movement of the plume are progressively dissolved, then the particulate component would create a plume denser than seawater that would then descend by the prevailing force of gravity. These two types of plumes were only observed during the 19 June 2012 operations (Fig. 2A). These plumes might correspond to vents sourced from the two types of hornitos identified on the ROV surveys near the summit; major pyramid-like chimneys at levels of 118–114 m (Fig. 5A) and tubular chimneys at 98–96 m water depth near the summit (Fig. 5D).

We suggest that the colloidal material might be composed of Fe-hydroxide flocculates; these flocculates are common with Fe-rich mats and can even detach from the seabed and move with the currents (Davis and Moyer, 2008). During the first ROV inspection of the volcano in April 2014, the summit of the volcano was covered by orange-brown, loosely packed Fe-oxide-rich flocculates that draped the entire surface (Somoza et al., 2017). Once magmatic activity subsided, hydrothermal activity beneath the hornitos directed the fluid (water and gas) to rise through fractures in the volcanic rocks (González et al., 2017).

5.2. Classification as hydrothermal mineralization

The hydrothermal origin of the Fe oxyhydroxides in Tagoro volcano is supported by their geological setting and mineralogical and chemical compositions. Typically, hydrothermal Fe-Mn-oxide deposits occur on the seafloor or below the water-sediment interface as stratabound layers and cement with a large fractionation between Fe and Mn (Hein et al., 1997; Koschinsky and Hein, 2003; Hein et al., 2005; González et al., 2016). They occur in many tectonic settings throughout the global ocean along the midoceanic ridges, back-arc basins, fracture zones, and intraplate seamounts and islands as is the case of Tagoro volcano. The oxides precipitate rapidly from low-temperature hydrothermal fluids (< 120 °C), which does not allow time for trace metals to be adsorbed by the precipitates. The maximum measured temperature of expelled fluids in Tagoro volcano was 39 °C (Hannington et al., 2016). These deposits are composed of poorly crystalline to amorphous Fe-Mn oxyhydroxides that can be enriched in certain metals like Mo, Zn, Pb, or Cu based on the composition of fluids, basement rocks leached, and formation of mineral deposits deeper in the hydrothermal system (Hein et al., 1997). The Fe-oxyhydroxide sediments from Tagoro volcano have a dendritic columnar texture, with an abundance of

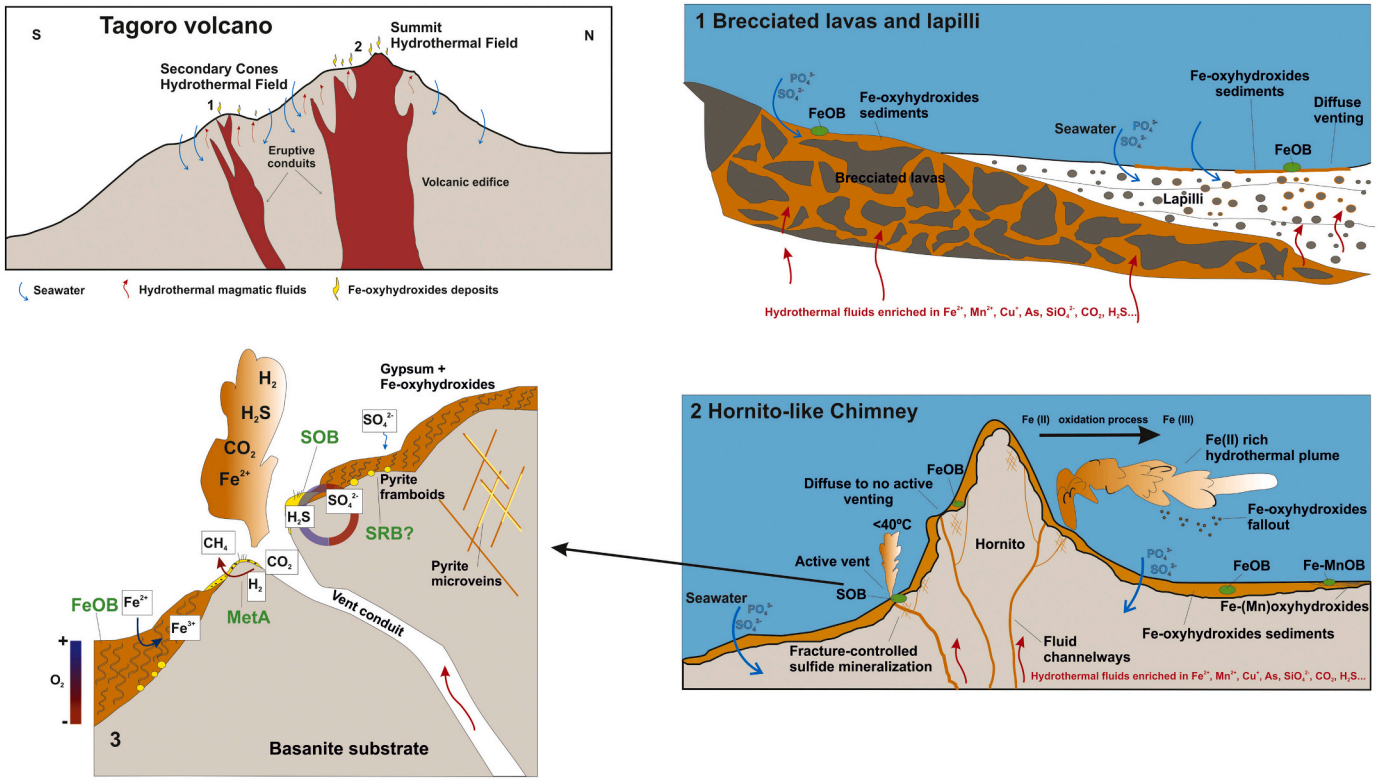

Fig. 13. Schematic model, not to scale, showing geologic setting and formation of Tagoro volcano hydrothermal deposits: (1) Secondary cones hydrothermal field with development of microbial-mediated Fe-oxyhydroxide mineralization on brecciated lavas and lapilli; (2) Summit hydrothermal field with mineralization on a hornito-like chimney; formation temperatures for the Fe-oxyhydroxide sediments are inferred to have varied below 40 °C; a host of elements (e.g., Fe, Si, P, Mn, As, Cu, Mo) were derived from leaching of basanite basement, sorbed from seawater, and to a lesser extent, magmatic fluids; Fe(II)-rich hydrothermal plumes allowed for the precipitation of Fe-Si-(Mn) mineralized sediments far away the vent sites; breakdown of the volcanic rock due to lava cooling or seismicity allowed for the precipitation of sulfides (pyrite ± chalcopyrite) from the hydrothermal fluids; (3): diversity of metabolic processes carried out by microorganisms related to diffuse venting. FeOB = iron-oxidizing bacteria, MetA = methanogenic archaea, SOB = sulfur-oxidizing bacteria, SRB = sulfate reducing bacteria.

poorly crystalline Fe oxyhydroxides (proto-ferrihydrite, ferrihydrite) and opal-A, high Fe/Mn ratios, low REY contents, negative Ce anomalies, positive Eu anomalies, and moderate to high As, Mo, Cu, V and Zn contents (Table 3; Fig. 10), as occur in many other modern hydrothermal deposits (e.g., Hein et al., 1997; Fitzgerald and Gillis, 2006; Hein et al., 2008b). Only two X-ray reflections, at 2.5 and 1.5 Å, indicate the beginning stage of crystallization for proto-ferrihydrite, whereas ferrihydrite shows five reflections at 2.52, 2.25, 1.97, 1.72 and 1.48 Å, as occur in other early-stage hydrothermal deposits (Pichler et al., 1999). The Fe-oxyhydroxide sediments plot in the hydrothermal field (Fig. 12A), at the almost pure Fe-rich endmember (Fe/Mn 7.3–816) on the Mn-Fe-(Co + Ni + Cu) x 10 ternary diagram (Bonatti et al., 1972; Lyle, 1981; Dymond et al., 1984). The lack of scavenging of trace metals (e.g., Co, Ce) from seawater (hydrogenetic deposition) is consistent with a pure hydrothermal origin. The very low REE/Fe ratios (< 0.0009) indicate rapid precipitation from hydrothermal solutions, and this ratio will be higher with time due to extended contact with seawater (Pichler et al., 1999). REE patterns of the mineralized samples have the characteristics of a low-temperature fluid (Fig. 11). In general, the mineralized sample/shale REE patterns indicate an integrated signal including a seawater component (negative Ce anomalies), hydrothermal components (slight positive Eu anomalies, low total REEs), and detrital volcanogenic phases especially in sample SV2/D16-R9ox (lack of strong Ce anomaly and high contents of Al, Ti, Sc) (Table 3 and Fig. 11). The higher total REY concentration in sample SV2/D16-R9ox must be due to the presence of small particles of volcaniclastic material (pyroxene detected by XRD) that was mixed in during Fe-oxyhydroxide precipitation. As support for this idea, the bedrock of these Fe-mineralized rocks shows very similar REY patterns to that of sample SV2/D16-R9ox. This detrital influence can also be evaluated from the Y/Ho ratios (26–31), which are within the range of basic volcanic rocks (mean 28), and hydrothermal ferromanganese deposits in the Pacific Ocean (Hein et al., 1997), rather than those of seawater (45–75, mean 57) (Bau, 1996). These Y/Ho ratios obtained for the Fe-oxyhydroxide sediments indicate that most of the REEs are associated with the volcaniclastic detrital fraction. A hydrogenetic contribution to Tagoro volcano oxyhydroxides can be considered negligible when compared to the markedly lower δ^{56}Fe and δ^{57}Fe values for purely hydrogenetic Fe-Mn crusts. The δ^{56}Fe obtained on FeMn crust DR16-14 from Tropic Seamount is −0.46‰ (Marino et al., 2019), consistent with isotopic values (−0.65 to −0.04‰) for other hydrogenetic Fe-Mn crusts (Levasseur et al., 2004). The positive δ^{56}Fe value (+0.38‰) obtained for hydrothermal sample SV2/D16R12ox is consistent with the δ^{56}Fe values for Fe oxyhydroxides and minerals precipitated in hydrothermally active areas from the Mid-Atlantic Ridge (Rouxel et al., 2004, 2018). Nevertheless, a minor seawater sorption component can be identified by the high P and U contents.

In addition, textural evidence also points to a hydrothermal origin. The dendritic columnar texture, as well as laminated textures, and presence of sulfides, are common in hydrothermal oxide deposits indicating physico-chemical variations during the growth of deposits (intensity of venting, pH, redox conditions, composition of fluids) (Hein et al., 1999, 2005, 2014). All these mineralogical and geochemical patterns indicate that these oxyhydroxides were directly precipitated from hydrothermal fluids with little sorption of dissolved phases from ambient seawater.

An increase of Na, Ca and Mg contents in a host volcanic rock is typically observed when hydrothermal alteration takes place (Pirajno,

2009). Furthermore, the longer the hydrothermal system is active, the more intensive are these chemical enrichments, but many different factors like type of host rock or weathering processes can control these enrichments. These enrichments are not detected in the collected samples from Tagoro volcano (Table 3), highlighting the recent onset of this hydrothermal system (after 2012).

5.3. The mineralization process

A system of permeable pathways through highly vesicular volcanic flows, pyroclastic deposits, fractures, and gravitational slides as the collapse event occurred in November 2011 (Somoza et al., 2017) should have promoted seawater circulation. Formation of convective cells across the volcanic edifice would place seawater in contact with hot rock producing reactions such as the leaching of metals (Fig. 13). The combination of heated modified seawater, containing residual magmatic gases (e.g., CO_2) and leached metals and Si, upon reaching the seafloor produces hydrothermal mineralization on or within the seafloor where mixed with cold seawater (e.g., Rona, 1984; Hannington et al., 2005; Pirajno, 2009). Fluctuations in pH and SO_4 and H_2S contents of the mineralizing fluids can lead to precipitation of different mineral phases. In this way, the presence of minute pyrite crystals forming a layer at the base of a thin lamina of Fe-oxyhydroxide sediment indicates higher fluid venting and more reducing conditions at the beginning of the hydrothermal mineral deposition. Alternatively, pyrite could have grown after Fe-oxyhydroxides formation by sealing of the vent micro-orifices, promoting reducing microenvironments for sulfide precipitation. Sulfides are scarce at Tagoro volcano but not totally absent and occur in other intraplate hotspot volcanic edifices (Hein et al., 1996). The fluids from these hotspot hydrothermal systems are poor in transitional metals and the fluids are less acid (pH = 5–6) than the spreading ridge deposits. However, these fluids are enriched in Fe, Mn, Si, Ba, and REEs when compared to seawater. Pyrite observed filling micro-cracks (veins and veintlets) within the basanite rock (Fig. 8C–D) indicates precipitation from hydrothermal fluids after lava cooling. The micro-cracks crosscutting magnetite, the groundmass and silicate phenocrysts indicate breakdown of the volcanic rock due to lava cooling or seismicity. This cracking of bedrock favors hydrothermal alteration of the basanite. Microcrystals of gypsum frequently covered by Fe oxyhydroxides on the surface of basanites (Fig. 9B) indicate rapid precipitation, before oxide precipitation. In the same way, minute anhydrite-gypsum crystals filling and surrounding vesicles within the basanite, and occasionally accompanied by pyrite and chalcopyrite (Fig. 8E–F), may have been associated with early precipitation at low pH. In summary, a more acidic and low-oxygenated environment can be interpreted as characteristic of the first phase of hydrothermal activity at Tagoro volcano, giving rise to deposition of sulfides and sulfates; a subsequent increase of pH and oxygenation promoted the precipitation Fe oxyhydroxides from the hydrothermal fluids that characterized the second phase.

A more complex formation of sulfide deposits within the Tagoro volcanic edifice cannot be discounted because of the hot metal-rich fluid circulation mixing with oxygenated and low-temperature seawater. Such deeper-seated sulfide deposits have been observed in intraplate edifices as a result of phreatomagmatic eruptions or tectonic fracturing (Hekinian, 2014), but may not be common in intraplate seamounts because of their high porosity and permeability (Hein et al., 1996). The scarce presence of sulfides in the studied samples is a common characteristic in other low-temperature hydrothermal Fe-oxyhydroxide deposits, where sulfides are frequently absent (e.g., Rona, 1984; Puteanus et al., 1991; Pichler et al., 1999). Precipitation of sulfide minerals in the sub-seafloor would remove sulfide from the hydrothermal fluids and consequently Fe oxyhydroxides would predominant the seafloor deposits (Fig. 13). Sulfuric-acid leaching of volcanic rocks results in extensive hydrothermal alteration and precipitation of kaolinite, jarosite, pyrite, or silica (opal-A) (e.g. Browne, 1991; Martínez-Frías, 1998; Jones et al., 2000; Martínez-Frías et al., 2004). Si is generally enriched in diffuse to focused hydrothermal fluids derived from higher-temperature reactions at depth, as noted for other submarine volcanoes and seamounts (DeCarlo et al., 1983; Frey and Clauge, 1983; Edwards et al., 2011).

Alteration of iron-bearing minerals like magnetite in the basanite rocks and direct precipitation from Fe^{2+}-rich hydrothermal solutions are the two processes that lead to the formation of Fe-oxyhydroxide deposits at Tagoro volcano. Fe^{3+} is absent in the vent fluids (Santana-González et al., 2017), therefore the rapid precipitation of low-crystalline Fe oxyhydroxides must be due to the oxidation of Fe^{2+} from the hydrothermal fluids by mixing with alkaline, cool and oxygenated seawater. Proto-ferrihydrite precipitated closer to the vent sites, and the precipitation of Mn-rich oxyhydroxides precipitated in more distal areas within a more oxidizing environment (Fig. 13). Mn^{2+} remains comparably longer in solution than Fe^{2+}, thus explaining its absence in the hornitos-like mineralization as proximal deposits; a distal deposit is only represented by sample SV2/D16-R15ox (Table 3 and Fig. 9D), and probably occurs in other areas away from the vent sites. At the same time, oxidizing conditions high enough to promote the precipitation of As-rich oxides, as for example in sample SV2/D16-R15ox, occurred at other shallow-water vent sites (Pichler et al., 1999).

5.4. The role of microorganisms in the mineralization

Microbial organisms are known to participate in the mineralization and precipitation of certain compounds as found at other hydrothermal vents (Emerson et al., 2007; Zeng et al., 2012). The precipitation includes metabolic processes directly (iron-oxidation, sulfate-reduction) or indirectly by the acceleration of mineralization promoted by the presence of microbial cells that act as nucleation sites, such as for opal-A (Urrutia & Beveridge, 1993; Fein et al., 2002; Phoenix et al., 2003; Konhauser et al., 2004; Hein et al., 2008a), or by providing a framework for the mineralization to take place (Hein et al., 2008a).

Columnar and laminar stromatolite-like growth of Fe-oxyhydroxide mineralization (Figs. 8B and 9A) commonly is mediated by diverse microbial communities that include bacteria, algae, and scattered fungi (Jones et al., 2000). Fe-oxyhydroxide films from Tagoro volcano express a columnar stromatolite-like structure when seen under the light microscope (Figs. 8 A-B). This structure, also known as frutexite, forms mainly metabolically by iron-oxidizing bacteria (Rodríguez-Martínez et al., 2011; Heim et al., 2017). SEM photomicrographs show filamentous to coccoidal textures in the studied Fe samples (Figs. 11 and 6S), described by numerous authors as biogenic Fe-oxyhydroxide deposits linked to the activity of microerophilic iron-oxidizing bacteria (FeOB) (Emerson and Moyer, 2002; Edwards et al., 2011). Additionally, iron isotopic signatures from sample SV2/D16-R12ox ($\delta^{56}Fe = +0.383$) support a biologically mediated Fe oxidation that promoting the precipitation of an oxide with the heavier Fe-isotope signature (Beard et al., 1999; Croal et al., 2004: Balci et al., 2006; Johnson et al., 2020).

The abundance of Fe-oxyhydroxide twisted stalks in the studied mats (Fig. 11A-B) and empty sheaths covered by Fe oxyhydroxides (Fig. 11D) indicate the mediation of bacteria in the of Fe^{2+} to Fe^{3+} from the hydrothermal fluids, promoting the rapid precipitation of oxides (Fig. 13). These twisted stalks are characteristic by-products of Zeta-proteobacteria *Mariprofundus ferrooxydans* (Emerson et al., 2007; Singer et al., 2011), although still unknown Zeta-proteobacteria may produce similar stalks. Empty straight sheaths observed in sample SV2/D16-R9ox (Fig. 11D) may as well be produced by unknown Zetaproteobacteria as a by-product of Fe-oxidation (Chan et al., 2016; Johannessen et al., 2017).

Environmental DNA analysis performed in Fe-oxyhydroxide sample SV2/D16-R11ox, revealed a low relative abundance of unknown Zetaproteobacteria (Table 6S). The disparity between the abundant Fe-oxyhydroxide stalks among the samples and the low number of reads

related to Zetaproteobacteria may indicate that the oxidation of Fe occurred during past events and hydrothermal fluids are no longer emitted through the sediment at those sites. Furthermore, most of the sequences related to sample SV2/D16-R11ox belong to *Marinomonas* sp. and *Candidatus* Nitrosopumilus (Fig. 5S). *Candidatus* Nitrosopumilus archaea have been proposed to interact with Zetaproteobacteria in the nitrogen cycle in iron mats recovered from the Troll Wall Vent Field (Arctic Gakkel Ridge; Vander Roost et al., 2017) and the Jan Mayen Vent Fields (Johannessen et al., 2017). However, in this study we find that their presence occurred during post Fe-oxidation colonization of the Fe mat by ubiquitous microorganisms that commonly thrive in the water column or hydrothermal vents, rather than an active interaction with iron-oxidizers. Thus, *Marinomonas* sp. (up to 52% relative abundance) and other taxa like Acidobacteria, Bacteroidetes, *Pseudoalteromonas* sp., Thermoplasmata, Woesearchaeota (DHVEG-6), and *Candidatus* Nitrosopelagicus (Walsh et al., 2016; Bergauer et al., 2018) are highly present in sample SV2/D16-R11ox.

Interestingly, sulfur-oxidizing bacteria constitute most of the remaining bacterial community (up to 19%) (Fig. 5S). These aerobic bacteria consume H_2S from the hydrothermal fluids or from the consumption of sulfate by sulfate-reducers (Fig. 13). *Desulfobulbus* Deltaproteobacteria represent 4.56% of the bacterial relative abundance, indicating the sulfur cycle was active in the Fe mat and participated in the precipitation of pyrite (Fig. 8A–B). These sulfur-related microorganisms, as well as methane-related microorganisms (i.e. methanogenic archaea and methanotrophic bacteria and archaea), also detected in sample SV2/D16-R11ox, are commonly found in Fe mats from low-temperature hydrothermal vents (Vander Roost et al., 2017). Sulfur-oxidizing bacterial mats are typically whitish with a flocculent-filamentous texture, like the ones that appear surrounding vent conduits in the external surface of the chimneys in the Tagoro volcano (Figs. 4C-E). While sulfur-oxidizing bacterial mats are normally found at higher temperature and related to chimney conduits (Fig. 13), Fe mats are found at lower temperature and more diffuse venting (Vander Roost et al., 2017).

Silicified microbial filamentous bodies (Fig. 11F) and other microbial-related structures covered by opal-A (Fig. 9E) are scattered among the samples from Tagoro volcano. Although it is unclear as to the active participation of microbial organisms in the silicification processes, a few studies have addressed the role of microbial surfaces in the rapid nucleation of opal-A and other silicates and minerals (Fortin et al., 1997; Boyd and Scott, 2001; Kelley et al., 2002; Hein et al., 2008a; Edwards et al., 2011). Furthermore, different studies suggested that Fe may favor the precipitation of silica (Fein et al., 2002; Hein et al., 2008a; Li et al., 2012).

Precise identification of the mineralized filamentous bodies, rod-shaped microorganisms, twisted stalks, and empty sheaths from Tagoro volcano is hindered in some samples by their simple architecture that lacks distinctive features that might clearly ally them with a particular taxon. Nevertheless, consideration of the microbial morphology, coupled with the known and inferred environmental conditions, allows inferences to be made about the possible taxonomic affinity of these microorganisms.

6. Summary and conclusions

The onset of hydrothermalism on Tagoro volcano (south Hierro Island, Canary Islands) was discovered in June 2012 from hydroacoustic flares, four months after the cessation of the submarine eruption. Two years after the 2012 eruption, a ROV dive imaged an active shallow-water hydrothermal vent system and secondary fissures at the summit. Changes in seawater physico-chemical parameters confirmed the existence of two areas with hydrothermal activity: i) the deepest zone (215-185 m water depth), where the secondary cones were found, and where mainly thermal anomalies were identified, and ii) close to the summit of the volcano (120-89 m water depth) where positive anomalies in T, CO_2, and fluorescence and negative anomalies in dissolved oxygen and salinity were measured. Three main types of mineralized structures are associated with the hydrothermal processes at different water depths: (1) 1-2 m high chimneys at 96-89 m water depth; (2) numerous up to 5 m-tall hornitos-like structures at water depths between 120 and 89 m built of iron- and silica-rich gelatinous deposits pooled over and between mafic lava spatter cones. Extensive deposits of Fe flocculates covered the summit seafloor. Vent structures showed the emission of high concentrations of CO_2 indicating that focused degasification was still active. Active focused emissions of hydrothermal fluids were identified by positive temperature and fluorescence anomalies, and negative dissolved oxygen and salinity anomalies; and (3) Fissure-type hydrothermal vents at the deepest zones (215–185 m depth) produced secondary cones opened during the latest stage of the eruption. In these deep vents, thermal anomalies were detected but concentrations of CO_2 were lower than emitted from the summit structures.

Fe oxyhydroxide formation in the Tagoro hydrothermal system (Fig. 13) took place during mixing of hydrothermal fluids with seawater, which gave rise to: (1) the precipitation of mostly Fe and minor Cu sulfides under reducing conditions, that occurred essentially subseafloor within the conduits or above the seafloor during venting of acidic/reduced fluids sourced from the hornitos; and (2) precipitation of amorphous Fe oxyhydroxides, opal-A, and sulfates probably from oxidation of Fe(II)-rich neutrally buoyant plumes at the oxic/photic zone, ~70-50 m water depths. Diverse microbial biota may have participated during the entire mineralization sequence, mainly Fe-oxidizing Zetaproteobacteria but also organisms involved in the sulfur and methane cycles. Rapid silicification of microbial-related structures may have been favored by microorganisms acting as nucleation sites or a framework for mineralization. In addition, the circulation of fluids in the fracture/feeder system precipitated sulfides as microveins and produced incipient alteration of the host rocks.

This hydrothermal system provides an excellent opportunity to study the formation of newly formed hydrothermal deposits and their association with microbiota at an intraplate hot-spot volcanic edifice under low-temperature, shallow-water conditions. The Tagoro volcano is the last hydrothermal system reported to date in the Canary Islands, and may be a modern analog of a seafloor iron umber deposit being generated. The discovery of this mineralization system and associated microbiota identifies a potential Fe-based chemosynthetic ecosystems, which typically have been studied at spreading centers and arc volcanoes. This discovery underscores the importance of geomicrobiological interactions in shaping mineral deposits on Earth today, and in the geological past. At a geological scale, volcanic eruptions and low-temperature hydrothermal vents might increase dissolved metals in seawater and generate extensive Fe-oxyhydroxide deposits.

Declaration of Competing Interest

None.

Acknowledgments

This work has been supported by the Spanish projects for the Extension of the Continental Shelf of Spain (CTM2010-09496-E), SUBVENT (CGL2012-39524-C02-02) and EXPLOSEA (CTM2016-75947-R); and the European projects EMODnet-Geology (EASME/EMFF/2018/1.3.1.8-Lot 1/SI2.811048) and H2020 GeoERA-MINDeSEA (Grant Agreement No. 731166, project GeoE.171.001). Thanks to the R/V *Sarmiento de Gamboa*, *Hesperides*, and ROV *Luso* crews for their effort during the *Gaire*, *Amuley*, *Subvent-1* and *Subvent-2* cruises in the El Hierro Island. We thanks to the Instituto Hidrográfico de la Marina for the multibeam data acquisition during the Spanish EEZ mapping project.

Appendix A. Supplementary data

Supplementary data to this article can be found online at https://doi.org/10.1016/j.margeo.2020.106333.

References

Alt, J.C., 1988. Hydrothermal oxide and nontronite deposits on seamounts in the eastern Pacific. Mar. Geol. 81, 227–239.

Ancochea, E., 2004. Canarias y el vulcanismo neógeno peninsular. In: Vera, J.A. (Ed.), Geología de España. SGE-IGME, Madrid, pp. 635–682.

Balci, N., Bullen, T.D., Witte-Lien, K., Shanks, W.C., Motelica, M., Mandernack, K.W., 2006. Iron isotope fractionation during microbially stimulated Fe (II) oxidation and Fe (III) precipitation. Geochim. Cosmochim. Acta 70 (3), 622–639. https://doi.org/10.1016/j.gca.2005.09.025.

Baturin, G.N., 1988. The Geochemistry of Manganese and Manganese Nodules in the Ocean. D. Riedel Publ. Co. 342 pp.

Bau, M., 1996. Controls on the fractionation of isovalent trace elements in magmatic and aqueous systems: Evidence from Y/Ho, Zr/Hf, and lanthanide tetrad effect. Contrib. Mineral. Petrol. 123, 323–333.

Bau, M., Schmidt, K., Koschinsky, A., Hein, J., Kuhn, T., Usui, A., 2014. Discriminating between different genetic types of marine ferro-manganese crusts and nodules based on rare earth elements and yttrium. Chem. Geol. 381, 1–9 10.1016/j.chemgeo.2014.05.004.

Beard, B.L., Johnson, C.M., Cox, L., Sun, H., Nealson, K.H., Aguilar, C., 1999. Iron isotope biosignatures. Science. 5435, 1889–1892. https://doi.org/10.1126/science. 285. 5435.1889.

Bergauer, K., Fernandez-Guerra, A., Garcia, J.A.L., Sprenger, R.R., Stepanauskas, R., Pachiadaki, M.G., Jensen, O.N., Herndl, G.J., 2018. Organic matter processing by microbial communities. Proc. Natl. Acad. Sci. U. S. A. 115, E400–E408.

Bonatti, E., Kraemer, T., Rydell, H., 1972. Classification and genesis of submarine iron-onmanganese deposits. In: Horn, D.R. (Ed.), Ferromanganese Deposits of the Ocean Floor. Arden House, New York, pp. 149–165.

Boyd, T.D., Scott, S.D., 2001. Microbial and hydrothermal aspects of ferric oxyhydroxides and ferrosic hydroxides: the example of Franklin Seamount, Western Woodlark Basin, Papua New Guinea. Geochem. Trans. 7, 45–56.

Browne, P.R.L., 1991. Mineralogical guides to interpreting the shallow paleohydrology of epithermal mineral depositing environments. In: Proceedings of the New Zealand Geothermal Workshop. 13. pp. 263–269.

Canet, C., Prol-Ledesma, R.M., Proenza, J.A., Rubio-Ramos, M.A., Forrest, M.J., TorresVera, M.A., Rodríguez-Díaz, A.A., 2005. Mn–Ba–Hg mineralization at shallow submarine hydrothermal vents in Bahía Concepción, Baja California Sur, Mexico. Chem. Geol. 224 (1-3), 96–112. https://doi.org/10.1016/j.chemgeo.2005.07.023.

Carmona, J., Romero, C., Dóniz, J., García, A., 2009. Siliceous alterations of the Montaña Señalo lavas, Timanfaya eruption (1730-1736) (Lanzarote, Canary Islands). Estud. Geol. 65 (1), 79–89. https://doi.org/10.3989/egeol.39709.050.

Carracedo, J.C., 1999. Growth, structure, instability and collapse of Canarian volcanoes and comparisons with Hawaiian volcanoes. J. Volcanol. Geotherm. Res. 94, 1–19. https://doi.org/10.1016/S0377-0273(99)00095-5.

Carracedo, J.C., Day, S., Gillou, H., Rodríguez, E., Canas, J.A., Pérez, F.J., 1998. Hotspot volcanism close to a passive continental margin: the Canary Islands. Geol. Mag. 135, 591–604.

Carracedo, J.C., Pérez, F.J., Ancochea, E., Meco, J., Hernán, F., Cubas, C.R., Casillas, R., Rodríguez, E., Ahijado, A., 2002. Cenozoic volcanism II: The Canary Islands. In: Moreno, T. (Ed.), Gibbons, W. The Geology of Spain, London, Geological Society of London, pp. 439–472.

Carracedo, J.C., Torrado, F.P., González, A.R., Soler, V., Turiel, J.L.F., Troll, V.R., Wiesmaier, S., 2012. The 2011 submarine volcanic eruption in El Hierro (Canary Islands). Geol. Today 28 (2), 53–58. https://doi.org/10.1111/j.1365-2451.2012.00827.x.

Carracedo, J.C., Troll, V.R., Zaczek, K., Rodríguez-González, A., Soler, V., Deegan, F.M., 2015. The 2011–2012 submarine eruption off El Hierro, Canary Islands: New lessons in oceanic island growth and volcanic crisis management. Earth Sci. Rev. 150, 168–200. https://doi.org/10.1016/j.earscirev.2015.06.007.

Chan, C.S., McAllister, S.M., Leavitt, A.H., Glazer, B.T., Krepski, S.T., Emerson, D., 2016. The architecture of iron microbial mats reflects the adaptation of chemolithotrophic iron oxidation in freshwater and marine environments. Front Microbiol. 7, 796.

Cherkashov, G., 2017. Seafloor massive sulfide deposits: distribution and prospecting. In: Sharma, R. (Ed.), Deep-Sea Mining: Resource Potential, Technical and Environmental Considerations. Springer International Publishing, Cham, Switzerland, pp. 143–164.

Croal, L.R., Johnson, C.M., Beard, B.L., Newman, D.K., 2004. In: Canfield, D.E. (Ed.), Iron isotope fractionation by Fe (II)-oxidizing photoautotrophic bacteria 1 1Associate. 68(6). Geochim. Cosmochim. Acta, pp. 1227–1242. https://doi.org/10.1016/j.gca.2003.09.011.

Danovaro, R., Canals, M., Tangherlini, M., Dell'Anno, A., Gambi, C., Lastras, G., Amblas, D., Sanchez-Vidal, A., Frigola, J., Calafat, A.M., Pedrosa-Pàmies, R., Rivera, J., Rayo, X., Corinaldesi, C., 2017. A submarine volcanic eruption leads to a novel microbial habitat. Nat. Ecol. Evol. 1, 0144. https://doi.org/10.1038/s41559-017-0144.

Davis, R.E., Moyer, C.L., 2008. Extreme spatial and temporal variability of hydrothermal microbial mat communities along the Mariana Island Arc and southern Mariana backarc system. J. Geophys. Res. 113 B08S15.

De Baar, H.J.W., de Jong, J.T.M., 2001. Distributions, sources and sinks of iron in seawater. In: Turner, D.R., Hunter, K.A. (Eds.), The Biogeochemistry of Iron in Seawater. John Wiley & Sons, Hoboken, N. Y.

DeCarlo, E.H., McMurtry, G.M., Yeh, H.-W., 1983. Geochemistry of hydrothermal deposits from the Loihi submarine volcano. Hawaii. Earth Planet. Sci. Lett. 66, 438–449.

Deegan, F.M., Troll, V.R., Barker, A.K., Harris, C., Chadwick, J.P., Carracedo, J.C., Delcamp, A., 2012. Crustal versus source processes recorded in dykes from the Northeast volcanic rift zone of Tenerife, Canary Islands. Chem. Geol. 334, 324–344.

Donoghue, E., Troll, V.R., Harris, C., O'Halloran, A., Walter, T.R., Torrado, F.J.P., 2008. Low-temperature hydrothermal alteration of intra-caldera tuffs, Miocene Tejeda caldera, Gran Canaria, Canary Islands. J. Volcanol. Geotherm. Res. 176, 551–564.

Dymond, J., Lyle, M., Finney, B., Piper, D.Z., Murphy, K., Conard, R., Pisias, N., 1984. Ferromanganese nodules from MANOP Sites H, S and R—control of mineralogical and chemical composition by multiple accretionary processes. Geochim. Cosmochim. Acta 48, 931–950.

Edwards, K.J., Glazer, B.T., Rouxel, O.J., Bach, W., Emerson, D., Davis, R.E., Toner, B.M., Chan, C.S., Tebo, B.M., Staudigel, H., Moyer, C.L., 2011. Ultra-diffuse hydrothermal venting supports Fe-oxidizing bacteria and massive umber deposition at 5000 m off Hawaii. International Society for Microbial Ecology 5, 1748–1758.

Emerson, D., Moyer, C.L., 2002. Neutrophilic Fe-oxidizing bacteria are abundant at the Loihi seamount hydrothermal vents and play a major role in Fe oxide deposition. Appl. Environ. Microbiol. 68, 3085–3093.

Emerson, D., Rentz, J.A., Lilburn, T.G., Davis, R.E., Aldrich, H., Chan, C., Moyer, C.L., 2007. A novel lineage of proteobacteria involved in formation of marine feoxidizing microbial mat communities. PLoS One 2 (7), 667. https://doi.org/10.1371/journal.pone.0000667.

Emerson, D., Fleming, E.J., McBeth, J.M., 2010. Iron-oxidizing bacteria: an environmental and genomic perspective. Annu. Rev. Microbiol. 64 (1), 561–583.

EMODnet, 2020. https://www.emodnet.eu/, Accessed date: 13 March 2020.

European Commission, 2017. COMMUNICATION FROM THE COMMISSION TO THE EUROPEAN PARLIAMENT, THE COUNCIL, THE EUROPEAN ECONOMIC AND SOCIAL COMMITTEE AND THE COMMITTEE OF THE REGIONS on the 2017 list of Critical Raw Materials for the EU. Brussels, 13.9.2017 COM(2017) 490 final.

Fein, J.B., Scott, S., Rivera, N., 2002. The effect of Fe on Si adsorption by Bacillus subtilis cell walls: insights into non- metabolic bacterial precipitation of silicate minerals. Chem. Geol. 182, 265–273.

Fitzgerald, C.E., Gillis, K.M., 2006. Hydrothermal manganese oxide deposits from Baby Bare seamount in the Northeast Pacific Ocean. Mar. Geol. 225, 145–156.

Fortin, D., Ferris, F.G., Beveridge, T.J., 1997. Surface-mediated mineral development by bacteria. In: Bandfield, J., Nealson, K.H. (Eds.), Geomicrobiology: interactions between microbes and minerals. Reviews in Mineralogy, vol. 35. Mineralogical Society of America, Washington, D.C, pp. 161–177.

Fraile-Nuez, E., González-Dávila, M., Santana-Casiano, J.M., Arístegui, J., Alonso-González, I.J., Hernández-León, S., Blanco, M.J., Rodríguez-Santana, A., Hernández-Guerra, A., Gelado-Caballero, M.D., Eugenio, F., Marcello, J., de Armas, D., Domínguez-Yanes, J.F., Montero, M.F., Laetsch, D.R., Vélez-Belchí, P., Ramos, A., Ariza, A.V., ComasRodríguez, I., Benítez-Barrios, V.M., 2012. The submarine volcano eruption at the island of El Hierro: physical-chemical perturbation and biological response. Sci. Rep. 2.

Frey, F.A., Clauge, D.A., 1983. Geochemistry of diverse basalt types from Loihi Seamount, Hawaii: petrogenetic implications. Earth Planet. Sci. Lett. 66, 337–355.

Geldmacher, J., Hoernle, K., van den Bogaard, P., Zankl, G., Garbe-Schönberg, D., 2001. Earlier history of the ≥70-Ma-old Canary hotspot based on the temporal and geochemical evolution of the Selvagen Archipelago and neighboring seamounts in the eastern North Atlantic. J. Volcanol. Geotherm. Res. 111 (1-4), 55–87. https://doi.org/10.1016/s03770273(01)00220-7.

Geldmacher, J., Hoernle, K., van den Bogaard, P., Duggen, S., Werner, R., 2005. New $^{40}Ar/^{39}Ar$ age and geochemical data from seamounts in the Canary and Madeira volcanic provinces. Earth Planet. Sci. Lett. 237, 85–101.

Gledhill, M., Buck, K.N., 2012. The organic complexation of iron in the marine environment: a review. Front. Microbiol. 3, 69. https://doi.org/10.3389/fmicb.2012.00069.

González, F.J., Somoza, L., Medialdea, T., León, R., Vázquez, J.T., Marino, E., Bellido, E., Reyes, J., 2014. Volcanism and ferromanganese deposits on seamounts and new volcanoes from the Canary Archipelago. IV Congress of Marine Sciences, At Las Palmas de Gran Canaria, Spain, Volume: Book of Abstracts Submitted to the IV Congress of Marine Sciences. 186 (ISBN-10: 84-697-0471-0; ISBN-13: 978-84-697-0471-4).

González, F.J., Somoza, L., Hein, J.R., Medialdea, T., León, R., Urgorri, V., Reyes, J., Martín-Rubí, J.A., 2016. Phosphorites, Co-rich Mn nodules, and Fe-Mn crusts from Galicia Bank, NE Atlantic: reflections of Cenozoic tectonics and paleoceanography. Geochem. Geophys. Geosyst. 17, 346–374. https://doi.org/10.1002/2015GC005861.

González, F.J., Rincón-Tomás, B., Somoza, L., Hein, J.R., Medialdea, T., Madureira, P., Reyes, J., Hoppert, M., Reitner, J., 2017. Fe-rich mineralized microbes from hydrothermal vents at Tagoro submarine volcano, El Hierro Island (central east Atlantic). In: Proceedings of the 113th Annual GSA Cordilleran Section Meeting-2017, Honolulu, HI, USA, 23–25 May.

Greinert, J., Artemov, Y., Egorov, V., De Batist, M., McGinnis, D., 2006. 1300-m-high rising bubbles from mud volcanoes at 2080 m in the Black Sea: Hydroacoustic characteristics and temporal variability. Earth Planet. Sci. Lett. 244 (1 – 2), 1–15.

Guillou, H., Carracedo, J.C., Perez Torrado, F., Rodriguez Badiola, E., 1996. K-Ar ages and magnetic stratigraphy of a hotspot-induced, fast grown oceanic island: El Hierro, Canary Islands. J. Volcanol. Geotherm. Res. 73, 141–155.

Halbach, M., Koschinsky, A., Halbach, P., 2001. Report on the discovery of Gallionella ferruginea from an active hydrothermal field in the deep sea. InterRidge news 10, 18–20.

Hanert, H.H., 2002. Bacterial and chemical iron oxide deposition in a shallow bay on Palaea Kameni, Santorini, Greece: microscopy, electron probe microanalysis, and photometry of in situ experiments. Geomicrobiol J. 19, 317–342.

Hannington, M.D., de Ronde, C.E.J., Petersen, S., 2005. Seafloor tectonics and submarine hydrothermal systems. Econ. Geol. 100th Ann. 111–141.
Hannington, M.D., Petersen, S., Santana-Casiano, M., Fraile-Nuez, E., Klischies, M., Lange, S., Hissman, K., Schauer, J., Striewski, P., Anderson, M.O., et al., 2016. POS-494 Leg 2 Cruise Report: Assessment of Ongoing Magmatic-Hydrothermal Discharge of the El Hierro Submarine Volcano, Canary Islands by the Submersible JAGO; RV POSEIDON. GEOMAR Helmholtz Centre for Ocean Research Kiel, Instituto de Oceanografia y Cambio Global. Instituto Español de Oceanografía: Kiel, Germany, p. 88.
Heim, C., Quéric, N.V., Ionescu, D., Schäfer, N., Reitner, J., 2017. Frutexites-like structures formed by iron oxidizing biofilms in the continental subsurface (Äspö Hard Rock Laboratory, Sweden). PLoS One 12 (5), e0177542. https://doi.org/10.1371/journal.pone.0177542.
Hein, J.R., Yeh, H.-W., Gunn, S.H., Gibbs, A.E., Wang, C.-H., 1994. Composition and origin of hydrothermal ironstones from central Pacific seamounts. Geochim. Cosmochim. Acta 58, 179–189.
Hein, J.R., Gibbs, A.E., Clague, D.A., Torresan, M., 1996. Hydrothermal mineralization along submarine rift zones. Hawaii. Mar. Georesour. Geotec. 14 (2), 177–203.
Hein, J.R., Koschinsky, A., Halbach, P., Manheim, F.T., Bau, M., Kang, J.-K., Lubick, N., 1997. Iron and manganese oxide mineralization in the Pacific. In: Nicholson, K., Hein, J.R., Buhn, B., Dasgupta, S. (Eds.), Manganese Mineralization: Geochemistry and Mineralogy of Terrestrial and Marine Deposits: Special Publication Geological Society of London, London. 119. pp. 123–138.
Hein, J.R., Koski, R.A., Embley, R.W., Reid, J., Chang, S.-W., 1999. Diffuse-flow hydrothermal field in an oceanic fracture zone setting, Northeast Pacific: Deposit composition. Explor. Min. Geol. 8, 299–322.
Hein, J.R., Koschinsky, A., Bau, M., Manheim, F.T., Kang, J.-K., Roberts, L., 2000. Cobaltrich ferromanganese crusts in the Pacific. In: Cronan, D.S. (Ed.), Handbook of marine minerals. CRC Press Boca Raton, Florida, pp. 239–279.
Hein, J.R., Koschinsky, A., McIntyre, B.R., 2005. Mercury- and silver-rich ferromanganese-oxides, Southern California Borderland: Deposit model and environmental implications, Econ. Geol. 100 (6), 1151–1168.
Hein, J.R., Clague, D.A., Koski, R.A., Embley, R.W., Dunham, R.E., 2008a. Metalliferous sediment and a silica-hematite deposit within the Blanco Fracture Zone, northeast Pacific. Mar. Georesour. Geotechnol. 26 (4), 317–339.
Hein, J.R., Schulz, M.S., Dunham, R.E., Stern, R.J., Bloomer, S.H., 2008b. Diffuse flow hydrothermal manganese mineralization along the active Mariana and southern IzuBonin arc system, western Pacific. J. Geophys. Res. 113https://doi.org/10.1029/2007JB005432. B08S14.
Hein, J.R., de Ronde, C.E.J., Koski, R.A., Ditchburn, R.G., Mizell, K., Tamura, Y., Stern, R.J., Conrad, T.A., Ishizuka, O., Leybourne, M.I., 2014. Layered hydrothermal barite-sulfide mound field, East Diamante caldera, Mariana volcanic arc. Econ. Geol. 109, 2179–2206.
Hekinian, R., 2014. Seafloor exploration. Scientific adventures diving into the abyss, Springer Oceanography 365 pp.
Hoernle, K., Tilton, G., Schmincke, H.U., 1991. SrNd-Pb isotopic evolution of Gran Canaria: evidence for shallow enriched mantle beneath the Canary Islands. Earth Planet. Sci. Lett. 106, 44–63.
Hoernle, K.A., Schmincke, H.U., 1993. The role of partial melting in the 15-Ma geochemical evolution of Gran Canaria: a blob model for the Canary hotspot. J. Petrol. 34, 599–626.
Hunter, K.A., Boyd, P.W., 2007. Iron-binding ligands and their role in the ocean biogeochemistry of iron. Environ. Chem. 4, 221–232.
IGN, Instituto Geográfico Nacional. 2012. https://www.youtube.com/watch?time_ continue = 9&v = bOUbqeolDdU&feature = emb_title (accessed 15 April 2020).
Instituto Geológico y Minero de España (IGME), 2014. Submission of Data and Information on the Limits of the Continental Shelf of Spain to the West of the Canary Islands, pursuant to Part VI and Annex II of United Nations Convention on the Law of the Sea. Inedited report.
Jannasch, H.W., 1995. Review lecture: The chemosynthetic support of life and the microbial diversity at deepsea hydrothermal vents. Proceedings of the Royal Society of London Series B, Biological Sciences. 225, 277–297.
Johannessen, K.C., Vander Roost, J., Dahle, H., Dundas, S.H., Pedersen, R.B., Thorseth, I.H., 2017. Environmental controls on biomineralization and Fe-mound formation in a low-temperature hydrothermal system at the Jan Mayen Vent Fields. Geochim. Cosmochim. Acta 202, 101–123. https://doi.org/10.1016/j.gca.2016.12.016.
Johnson, C., Beard, B., Weyer, S., 2020. High-Temperature Fe Isotope Geochemistry. In: In: Iron Geochemistry: An Isotopic Perspective. Springer, Cham, Advances in Isotope Geochemistry.
Jones, B., Renaut, R.W., Rosen, M.R., 2000. Stomatolites forming in acidic hot-spring waters, North Island, New Zealand. Palaios 15 (5), 450–475.
Juniper, S.K., Tebo, B.M., 1995. Microbe-metal interactions and mineral deposition at hydrothermal vents. In: Karl, D.M. (Ed.), The Microbiology of Deep-Sea Hydrothermal Vents. CRC Press, New York, pp. 219–253.
Karl, D.M., McMurtry, G.M., Malahoff, A., Garcia, M.O., 1988. Loihi seamount, Hawaii—a mid-plate volcano with distinct hydrothermal system. Nature 335, 532–535.
Kelley, D.S., Baross, J.A., Delaney, J.R., 2002. Volcanoes, fluids and life at Mid-ocean ridge spreading centers. Annu. Rev. Earth Planet. Sci. 30, 385–491.
Klindworth, A., Pruesse, E., Schweer, T., Peplies, J., Quast, C., Horn, M., Glöckner, F.O., 2013. Evaluation of general 16S ribosomal RNA gene PCR primers for classical and nextgeneration sequencing-based diversity studies. Nucleic Acids Res. 41, e1.
Klügel, A., Hansteen, T.H., van den Bogaard, P., Strauss, H., Hauff, F., 2011. Holocene fluid venting at an extinct Cretaceous seamount, Canary archipelago. Geology 39, 855–858.
Konhauser, K. O., Jones, B., Phoenix, V. R., Ferris, F. G., and Renaut, R. W., 2004. The microbial role in hot spring silicification. Ambio, 33, 552–558.
Koschinsky, A., Hein, J.R., 2003. Uptake of elements from seawater by ferromanganese crusts: solid-phase associations and seawater speciation. Mar. Geol. 198 (3–4), 331–351. https://doi.org/10.1016/S0025-3227(03)00122-1.
Le Maitre, R.W., Bateman, P., Dudek, A., Keller, J., Lameyre, J., Le Bas, M.J., Sabine, P.A., Schmid, R., Sorensen, H., Streckeisen, A., Woolley, A.R, Zanettin, B., 1989. A Classification of Igneous Rocks and Glossary of Terms: Recommendations of the International Union of Geological Sciences Subcommission on the Systematics of Igneous Rocks, 193 pp. In: Blackwell Sci. U. K, Oxford.
León, R., Somoza, L., Urgeles, R., Medialdea, T., Ferrer, M., Biain, A., García-Crespo, J., Mediato, J.F., Galindo, I., Yepes, J., González, F.J., Giménez-Moreno, J., 2017. Multievent oceanic island landslides: new onshore-offshore insights from El Hierro Island, Canary Archipelago. Mar. Geol. 393, 156–175 10.1016/j.margeo.2016.07.001.
León, R., Palomino, D., Vázquez, J.-T., Medialdea, T., Somoza, L., 2019. A new scenario for the mass transport deposits west Canary volcanic province. Earth Planet. Sc. Lett. 509, 27–37. https://doi.org/10.1016/j.epsl.2018.12.020.
Levasseur, S., Frank, M., Hein, J.R., Halliday, A.N., 2004. The global variation in the iron isotope composition of marine hydrogenetic ferromanganese deposits: implications for seawater chemistry? Earth Planet. Sc. Lett. 224, 91–105. https://doi.org/10.1016/j.epsl.2004.05.010.
Li, J., Zhou, H., Peng, X., Wu, Z., Chen, S., Fang, J., 2012. Microbial diversity and biomineralization in low-temperature hydrothermal iron–silica-rich precipitates of the Lau Basin hydrothermal field. FEMS microbiol. Ecol. 81 (1), 205–216.
Longpré, M.-A., Troll, V.R., Walter, T.R., Hansteen, T.H., 2009. Volcanic and geochemical evolution of the teno massif, tenerife, Canary Islands: Some repercussions of giant landslides on ocean island magmatism. Geochem. Geophys. Geosyst. 10 Q12017.
López, C., Blanco, M.J., Abella, R., Brenes, B., Cabrera Rodríguez, V.M., Casas, B., Domínguez Cerdeña, I., Felpeto, A., Fernández de Villalta, M., del Fresno, C., García, O., García-Arias, M.J., García-Cañada, L., Gomis Moreno, A., GonzálezAlonso, E., Guzmán Pérez, J., Iribarren, I., López-Díaz, R., Luengo-Oroz, N., Meletlidis, S., Moreno, M., Moure, D., Pereda de Pablo, J., Rodero, E., Romero, E., Sainz-Maza, S., Sentre Domingo, M.A., Torres, P.A., Trigo, P., Villasante-Marcos, V., 2012. Monitoring the volcanic unrest of El Hierro (Canary Islands) before the onset of the 2011–2012 submarine eruption, Geophys. Res. Lett., 39, L13303.
Lyle, M., 1981. Formation and growth of ferromanganese oxides on the Nazca plate. In: Kulm, L.D., Dymond, J., Dasch, E.J., Hussong, D.M. (Eds.), Nazca Plate: Crustal Formation and Andean Convergence. Geol. Soc. Am. Mem, vol. 154. pp. 269–293.
Mangas, J., Pérez Torrado, F.J., Reguilón, R., Martín-Izard, A., 1994. Metalogenia de las mineralizaciones de tierras raras asociadas a los complejos intrusivos alcalinocarbonáticos de Fuerteventura, islas Canarias. In: Rey, J., Martínez-Frías, J., Lunar, R. (Eds.), Geología y Metalogenia en ambientes oceánicos. Depósitos Hidrotermales Submarinos, Publicaciones Especiales del Instituto Español de Oceanografía, I, pp. 71–81.
Marino, E., González, F.J., Somoza, L., Lunar, R., Ortega, L., Vázquez, J.T., Reyes, J., Bellido, E., 2017. Strategic and rare elements in CretaceousCenozoic cobalt-rich ferromanganese crusts from seamounts in the Canary Island Seamount Province (northeastern tropical Atlantic), Ore Geol. Rev. 87, 21–41. https://doi.org/10.1016/j.oregeorev.2016.10.005.
Marino, E., González, F.J., Kuhn, T., Madureira, P., Wegorzewski, A.V., Mirao, J., Medialdea, T., Oeser, M., Miguel, C., Reyes, J., Somoza, L., Lunar, R., 2019. Hydrogenetic, Diagenetic and Hydrothermal Processes Forming Ferromanganese Crusts in the Canary Island Seamounts and Their Influence in the Metal Recovery Rate with Hydrometallurgical Methods. Minerals 9 (7), 439 doi:10.3390/min9070439.
Martínez-Frías, J., 1998. An ancient Ba-Sb-Ag-Fe-Hg-bearing hydrothermal system in SE Spain. Episodes 21-4, 248–252.
Martínez-Frías, J., Lunar, R., Rodríguez-Losada, J., Delgado, A., Rull, F., 2004. The volcanism-related multistage hydrothermal system of El Jaroso (SE Spain): Implications for the exploration of Mars. Earth Planets Space 56 (7), v–viii.
Medialdea, T., Somoza, L., González, F.J., Vázquez, J.T., de Ignacio, C., Sumino, H., Sánchez-Guillamón, O., Orihashi, Y., León, R., Palomino, D., 2017. Evidence of a modern deep water magmatic hydrothermal system in the Canary Basin (eastern central Atlantic Ocean). Geochem. Geophys. Geosyst. 18 (8), 3138–3164. https://doi.org/10.1002/2017gc006889.
Michard, H.W., Michard, G., Javoy, M., Cheminée, J.-L., Binard, N., 1989. Chemistry of submarine springs from the Teahitia seamount. EOS. Trans. Am. Geophys. Union 70, 495.
MINDeSEA, 2020. https://geoeramindesea.wixsite.com/mindesea, Accessed date: 3 May 2020.
Moeller, K., Schoenberg, R., Grenne, T., Thorseth, I.H., Drost, K., Pedersen, R.B., 2014. Comparison of iron isotope variations in modern and Ordovician siliceous Fe oxyhydroxide deposits. Geochim. Cosmochim. Acta 126, 422–440. https://doi.org/10.1016/j.gca.2013.11.018.
Movahednia, M., Rastad, E., Rajabi, A., Maghfouri, S., González, F.J., Alfonso, P., Choulet, F., Canet, C., 2020. The Ab-Bagh Late Jurassic-Early Cretaceous sediment-hosted Zn-Pb deposit, Sanandaj-Sirjan zone of Iran: Ore geology, fluid inclusions and (S–Sr) isotopes. Ore Geol. Rev. 121, 103484. https://doi.org/10.1016/j.oregeorev.2020.103484.
Oeser, M., Weyer, S., Horn, I., Schuth, S., 2014. High-precision fe and mg isotope ratios of silicate reference glasses determined in situ by femtosecond LA-MC-ICP-MS and by solution nebulisation MC-ICP-MS. Geostand. Geoanal. Res. 38, 311–328. https://doi.org/10.1111/j.1751-908X.2014.00288.x.
Palme, H., Schultz, L., Spettel, B., Weber, H.W., Wänke, H., Christophe, Michel-Levy M., Lorin, J.C., 1981. The Acapulco meteorite: Chemistry, mineralogy, and irradiation effect. Geochim. Cosmochim. Acta 45, 727–752.
Phoenix, V. R., Konhauser, K. O., and Ferris, F. G., 2003. Experimental study of iron and silica immobilization by bacteria in mixed Fe-Si systems: implications for microbial

silicification in hot-springs. Canadian Journal of Earth Sciences, 40, 1669–1678.
Pichler, T., Veizer, J., Hall, G.E.M., 1999. Natural input of arsenic into a coral-reef ecosystem by hydrothermal fluids and its removal by Fe III oxyhydroxides. Environ. Sci. Technol. 33 (9), 1373–1378.
Pirajno, F., 2009. Hydrothermal Processes and Mineral Systems. Springer/Geological Survey of Western Australia. 1250 pp.
Puteanus, D., Glasby, G.P., Stoffers, P., Kunzendorf, H., 1991. Hydrothermal iron-rich deposits from the Teahitia-Mehitia and Macdonald hot spot areas. Mar. Geol. 98, 389409.
Resing, J.A., Sedwick, P.N., German, C.R., et al., 2015. Basin-scale transport of hydrothermal dissolved metals across the South Pacific Ocean. Nature 523 (7559), 200–203. https://doi.org/10.1038/nature14577.
Rincón-Tomás, B., Duda, J.-P., Somoza, L., González, F.J., Schneider, D., Medialdea, T., Santofimia, E., López-Pamo, E., Madureira, P., Hoppert, M., Reitner, J., 2019. Cold-water corals and hydrocarbon-rich seepage in Pompeia Province (Gulf of Cádiz) – living on the edge. Biogeosciences 16 (7), 1607–1627.
Robertson, A.H.F., 1975. Cyprus umbers: basalt-sediment relationships on a Mesozoic ocean ridge. J. Geol. Soc. Lond. 131, 511–531.
Rodríguez-Losada, J.A., Martínez-Frías, J., Bustillo, M.A., Delgado, A., HernándezPacheco, A., de la Fuente Krauss, J.V., 2000. The hydrothermally altered ankaramite basalts of Punta Poyata (Tenerife, Canary Islands). J. Volcanol. Geotherm. Res. 103, 367–376.
Rodríguez-Martínez, M., Heim, C., Quéric, N.V., Reitner, J., 2011. Frutexites. In: Thiel, V. (Ed.), Reitner, J. Springer, Encyclopedia of Geobiology, pp. 396–400.
Rona, P.A., 1986. Mineral deposits from seafloor hot springs. Sci. Am. 254, 66–75.
Rona, P.A., 2003. Resources of the seafloor. Science 299, 673–674.
Rona, P.A., Bostrom, K., Laubier, L., Smith, K.L., 1983. Hydrothermal processes at seafloor spreading centers. Plenum, New York 796 pp.
Rona, P.A., 1984. Hydrothermal mineralization at seafloor spreading centers. Earth Sci. Rev., 20, pp. 1-104.
Rouxel, O., Fouquet, Y., Ludden, J.N., 2004. Subsurface processes at the lucky strike hydrothermal field, Mid-Atlantic ridge: evidence from sulfur, selenium, and iron isotopes. Geochim. Cosmochim. Acta 68 (10), 2295–2311. https://doi.org/10.1016/j.gca.2003.11.029.
Rouxel, O., Toner, B., Germain, Y., Glazer, B., 2018. Geochemical and iron isotopic insights into hydrothermal iron oxyhydroxide deposit formation at Loihi Seamount. Geochim. Cosmochim. Acta 220, 449–482. https://doi.org/10.1016/j.gca.2017.09.050.
Santana-Casiano, J.M., González-Dávila, M., Fraile-Nuez, E., de Armas, D., González, A.G., et al., 2013. The natural ocean acidification and fertilization event caused by the submarine eruption of El Hierro. Sci. Rep. 3, 1140.
Santana-Casiano, J.M., Fraile-Nuez, E., González-Dávila, M., Baker, E.T., Resing, J.A., Walker, S.L., 2016. Significant discharge of CO2 from hydrothermalism associated with the submarine volcano of El Hierro Island. Nat. Sci. Rep. 6, 25686. https://doi.org/10.1038/srep25686.
Santana-Casiano, J.M., González-Dávila, M., Fraile-Nuez, E., 2018. The Emissions of the Tagoro Submarine Volcano (Canary Islands, Atlantic Ocean): Effects on the physical and chemical properties of the seawater. In: Volcanoes: geological and geophysical setting, theoretical aspects and numerical modeling, applications to Industry and Their Impact on the Human Health, pp. 53–72.
Santana-González, C., Santana-Casiano, J.M., González-Dávila, M., Fraile-Nuez, E., 2017. Emissions of Fe (II) and its kinetic of oxidation at Tagoro submarine volcano, El Hierro. Mar. Chem. 195, 129–137.
Schiffman, P., Staudigel, H., 1994. Hydrothermal alteration of a seamount Complex on La Palma. Canary Islands. Implications for metamorphism in accreted terranes. Geology 2, 151–154.
Schmincke, H.U., 1982. Volcanic and chemical evolution of the Canary Islands. In: Von Rad, U., Hinz, K., Sarnthein, M., Seibold, E. (Eds.), Geology of the Northwest African margin. Springer, Berlin, pp. 273–306.
Singer, E., Emerson, D., Webb, E.A., Barco, R.A., Kuenen, J.G., Nelson, W.C., Heidelberg, J.F., 2011. Mariprofundus ferrooxydans PV-1 the first genome of a marine Fe (II) oxidizing Zetaproteobacterium. PLoS One 6 (9), e25386.
Somoza, L., Vázquez, J.T., Campos, A., Afonso, A., Calado, A., Fernández Puga, M.C., González Sanz, F.J., Fernández-Salas, L.M., Ferreira, M., Sanchez Guillamón, O., López Pamo, E., Lourenço, N., Luque Gómez, V., Mamouni, A., Medialdea, T., Madureira, P., Palomino, D., Rincón Tomás, B., Roque, C., Santos Bettencourt, R.P., Toyos Simón, M., 2014. Informe Científico-Técnico Campaña SUBVENT-2 (CGL2012-39524-C02). http://info.igme.es/SidPDF/166000/941/166941_0000001.pdf.
Somoza, L., González, F.J., Barker, S.J., Madureira, P., Medialdea, T., de Ignacio, C., Lourenço, N., León, R., Vázquez, J.T., Palomino, D., 2017. Evolution of submarine eruptive activity during the 2011-2012 El Hierro event as documented by hydroacoustic images and remotely operated vehicle observations. Geochem. Geophys. Geosyst. 18, 3109–3137.
Sovacool, B., Saleem, A., Morgan, B., Radley, B., Nemery, B., Okatz, J., Mulvaney, D., 2020. Sustainable minerals and metals for a low-carbon future. Science. 367, 30–33. https://doi.org/10.1126/science.aaz6003.
Staudigel, H., Feraud, G., Giannerini, G., 1986. The history of intrusive activity on the island of La Palma (Canary Islands). Jour. Volcanol. Geotherm. Res. 27, 299–322.
Stoffers, P., Glasby, G.P., Stüben, D., Renner, R.M., Pierre, T.G., Webb, J., Cardile, C.M., 1993. Comparative mineralogy and geochemistry of hydrothermal iron-rich crusts from the Pitcairn, Teahitia-Mehetia, and Macdonald hot spot areas of the S.W. Pacific. Mar. Geores. Geotechn. 11, 45–86.
Taylor, S.R., McLennan, S.M., 1985. The Continental Crust; Its Composition and Evolution; an Examination of the Geochemical Record Preserved in Sedimentary Rock. 312 Blackwell, Oxford.
Theis, T.L., Singer, P.C., 1974. Complexation of iron (II) by organic matter and its effect on iron (II) oxygenation. Environ. Sci. Technol. 8, 569–573.
Tornos, F., Peter, J.M., Allen, R., Conde, C., 2015. Controls on the siting and style of volcanogenic massive sulphide deposits: Ore Geol. Rev. 68, 142–163.
Tornos, F., Oggerin, M., De los Ríos, A., Rodríguez, N., Amils, R., Sanz, J.L., Rojas, P., Velasco, F., Escobar, J.M., Gómez, C., Slack, J.F., 2018. Do microbes control the formation of giant copper deposits? Geology. 47 (2), 143–146. https://doi.org/10.1130/G45573.1.
Turekian, K.K., Wedepohl, KH., 1961. Distribution of the Elements in some major units of the Earth's crust. Geological Society of America, Bulletin. 72, 175–192.
Urrutia, M.M., Beveridge, T.J., 1993. Remobilization of heavy metals retained as oxyhydroxides or silicates by Bacillus subtilis cells, Appl. Environ. Microbiol. 59, 4323–4329.
Van den Bogaard, P., 2013. The origin of the Canary Island Seamount Province —New Ages of Old Seamounts. Sci. Rep. 3, 2107. https://doi.org/10.1038/srep02107.
Van Dover, C., 2000. The ecology of deep-sea hydrothermal vents. Princeton University Press 448 pp.
Vander Roost, J., Thorseth, I.H., Dahle, H., 2017. Microbial analysis of Zetaproteobacteria and co-colonizers of iron mats in the Troll Wall Vent Field, Arctic Mid-Ocean Ridge. PLoS One 12 (9), e0185008. https://doi.org/10.1371/journal.pone.0185008.
Walsh, E.A., Kirkpatrick, J.B., Rutherford, S.D., Smith, D.C., Sogin, M., D'Hondt, S., 2016. Bacterial diversity and community composition from seasurface to subseafloor. ISME J. 10, 979–989.
Wemheuer, F., von Hoyningen-Huene, A.J.E., Pohlner, M., Degenhard, J., Engelen, B., Daniel, R., Wemheuer, B., 2019. Primary Production in the water column as major structuring element of the biogeographical distribution and function of Archaea in deepsea sediments of the Central Pacific Ocean. Archaea 2019, 3717239.
Weyer, S., Schwieters, J., 2003. High precision Fe isotope measurements with high mass resolution MC-ICPMS. Int. J. Mass Spectrom. 226 (3), 355–368. https://doi.org/10.1016/s13873806(03)00078-2.
Zeng, Z., Ouyang, H., Yin, X., Chen, S., Wang, X., Wu, L., 2012. Formation of Fe-Si-Mn oxyhydroxides at the PACMANUS hydrothermal field, eastern Manus basin: Mineralogical and geochemical evidence. Journal of Asian Earth Sciences 60, 130–146.